Studies of the effects of non-linear materials in the CREX septum magnet using finite element analysis simulations

by

Iris Halilovic

A thesis submitted to
The Faculty of Graduate Studies of
The University of Manitoba
in partial fulfillment of the requirements
of the degree of

Master of Science

Department of Physics and Astronomy
The University of Manitoba
Winnipeg, Manitoba, Canada
January 2022

Thesis advisor
Juliette Mammei

Author
Iris Halilovic

Studies of the effects of non-linear materials in the CREX septum magnet using finite element analysis simulations

Abstract

The CREX experiment measures the ^{48}Ca neutron radius using an electroweak probe. To run the experiment after PREX-2, which measures the neutron radius of ^{208}Pb with the same electroweak parity violation technique, without a configuration change of the equipment, the septum magnet needs to meet field requirements suitable for CREX. As the magnet is iron-dominated the field response is non-linear at sufficiently high current. This is of particular concern for CREX which is run at a beam energy more than double that of PREX-2 and requires a large septum current to provide the specified bend radius. To determine it's suitability in the experiment the magnet non-linearity must be characterized. To that end, the magnetic flux density was simulated using finite element analysis software and was analyzed in the high-field regions and the zero-field region of the septum. In this thesis I will show evidence of magnetic saturation in the septum magnet at the CREX current and that the requisite field strength can be attained in the magnet gaps. I will also show that the proposed upstream and downstream extensions of the beam pipe shield reduce the maximum fringe field strength by more than 80% and provide a factor of 10 improvement to the maximum field integral inside the beam pipe region.

Acknowledgments

I'd like to thank my advisor Juliette Mammei for her advice on various aspects of this process, reading the thesis drafts, and meeting to discuss the simulations and analysis. I also greatly appreciate the efforts of the examination committee members Gerald Gwinner and Michael Gericke. Thank you for your time and the helpful comments on the thesis. Thanks, also, to the engineers and staff scientists at Jefferson Lab, in particular Jay Benesch and Robin Wines.

Thank you to Susan Beshta, Robyn Beaulieu, and Maiko langelaar for the wonderful support they provide to the department, without which would have made my graduate studies more difficult.

To my partner, family, and friends, your love and support is very meaningful to me. Will, I couldn't have completed this thesis without your support. Thank you, for reading my drafts and providing your helpful comments, and for being your awesome self.

This thesis is dedicated to my loving parents.

Contents

List of Tables

List of Figures

I. Introduction

A. Scientific Context and Motivation

1) Study of Neutron Densities using an Electroweak Probe: Present understanding of the structure of atomic nuclei predominantly arises from accurate, model-independent measurements of nuclear charge densities from electron scattering experiments which probe nuclei via the electromagnetic interaction [1]. However important these experiments have been to our knowledge of the sizes and shapes of nuclei, electron scattering is limited in that this technique does not directly probe the neutron densities of atomic nuclei because neutrons are electrically neutral. This has relevance for the structure of neutron rich nuclei, for which the measured radial charge distribution alone is insufficient to determine the size of the nucleus due to the presence of a neutron skin at the surface, an expected feature of nuclei with neutron excess [2]; the neutron skin is defined as the difference between the neutron (R_n) and proton (R_p) root-mean-square (rms) radii, $\Delta R_{np} = R_n - R_p$.

Measurements of R_n have been predominately deduced from hadron scattering experiments but these results are model-dependent due to theoretical uncertainties in the strong interactions and are generally not accepted by the field [3]. An alternate method of probing neutron densities is with parity violating electron scattering (PVES), which, as Horowitz *et al* show in [2], can be used to extract an R_n measurement with relatively small theoretical uncertainties. This technique probes fixed-target, unpolarized nuclei by longitudinally polarized electron scattering via the weak interaction and measures the parity-violating asymmetry A_{LR} of the scattering probabilities of left- and right-handed electrons defined as

$$A_{LR} = \frac{\sigma_R - \sigma_L}{\sigma_R + \sigma_L}, \tag{1}$$

where $\sigma_{R(L)}$ is the elastic scattering cross-section of right (left) handed electrons [1]. This is sensitive to the neutron distribution because the weak charge of the neutron is much larger than that of the proton. In the Born approximation at low Q^2 (the square of the four-momentum transfer) the asymmetry is given by [2],

$$A_{LR} \approx \frac{G_F Q^2}{4\pi\alpha\sqrt{2}} \frac{F_n(Q^2)}{F_p(Q^2)}, \tag{2}$$

where G_F is the Fermi constant, α the fine structure constant, $F_p(Q^2)$ is the known proton nuclear form factor, and $F_n(Q^2)$ is the unknown neutron nuclear form factor. By measuring A_{LR}, one measures the neutron form factor from which R_n can be extracted since $F_n(Q^2)$ is the Fourier transform of the neutron density $\rho_n(r)$.

2) PVES Experimental Technique at JLab: The accelerator facility at Jefferson Lab delivers a stable, highly longitudinally polarized (∼89%) electron beam to experimental Hall A. At the polarized electron source, the beam helicity is rapidly reversed at a frequency of 120 or 240 Hz. The helicity sign of the electron beam is constant for a ∼8 ms window, referred to as a helicity window, and either positive or negative, that is, the electron spin points in the direction that is either parallel (right-handed electron) or antiparallel (left-handed electron), respectively, to the direction of beam propagation. In Hall A, the beam is transported by a system of magnets to the interaction point - a fixed-target of unpolarized nuclei - and scattered by the target. Downstream of the interaction point, the elastically scattered electrons are separated from the inelastic peak by the High Resolution Spectrometer (HRS) arms and are focused onto the main quartz detectors. See Fig.1. for a schematic of this process. The scattered electron flux is measured by analog integration of the main detector signals over each helicity window [4]. A_{PV}^{meas} is the fractional difference of the detector yield in the two helicity states,

$$A_{PV}^{meas} = \frac{Y_+ - Y_-}{Y_+ + Y_-}, \tag{3}$$

where $Y_{+(-)}$ is the main detector yield in the $+(-)$ helicity state, and is measured for each pattern flip sequence (a quartet pattern in the case of 120 Hz helicity reversal, where the flip sequence is either $+--+$ or its complement).

Fig. 1. Schematic of elastic electron focusing. The elastically scattered electrons are focused onto the downstream main detectors by the HRS while the inelastic peak is separated.

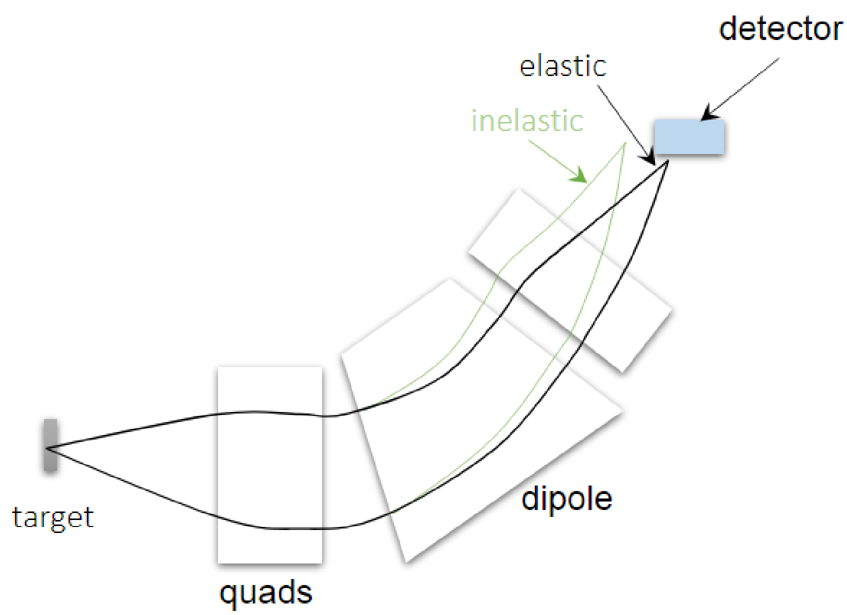

3) ^{208}Pb and ^{48}Ca as Target Nuclei: The PVES experimental technique for studying bulk neutron properties was first demonstrated by PREX-1 (the Lead Radius Experiment) at Jefferson Lab, which measured the ^{208}Pb neutron rms radius using a purely electroweak probe and observed its neutron skin of $0.33^{+0.16}_{-0.18}$ fm thickness [5]. PREX-1 achieved the proposed systematic uncertainty, but precision of the measurement was limited by statistics due to low running efficiency, which was caused by problems with radiation and the vacuum system [6]. A 1% measurement of $R_n(^{208}\mathrm{Pb})$ will further constrain mean field interactions in nuclear theory [2] and have implications on the structure of neutron stars due to information it can provide on the EOS of neutron matter [3]. To obtain the requisite precision a follow-up experiment PREX-2 was approved to accumulate more statistics and thereby reduce the total experimental uncertainty of the measurement.

While PREX-2 will provide experimental input that can be related to bulk properties of neutron-rich matter, R_n of a light-mass, neutron-rich nucleus will provide insight toward bridging nuclear DFT and ab-initio theoretical approaches to describe hadronic systems [7]. To this end, Ban *et al* [3] examined several of such nuclei to determine their suitability as a target in an experiment similar to PREX-2, to be run in Hall A at Jefferson Lab. A candidate nucleus, ^{48}Ca, was selected for the CREX experiment [7].

Because the size of A_{PV} is typically on the order of a part per million (ppm) [4], high count rates are required to obtain meaningful statistics in the measurement. However, at a fixed energy and Q^2, the count rate decreases rapidly with the scattering lab angle, θ, while A_{PV} grows with increasing θ thus requiring an optimization of experimental parameters. An example of this is shown in Fig.2. and Fig.3. for a ^{48}Ca target and a beam current of 100 μA at 2.2 GeV. I did not run the monte carlo simulation to produce these figures, they belong to the PREX collaboration and were generously provided by my advisor, Dr. Mammei.

Fig. 2. Rate vs. scattering angle. The rate of electrons elastically scattered off the ^{48}Ca target vs. scattering angle. The rate is for a 100 μA beam at 2.2 GeV and is averaged over the acceptance of the HRS and septum.

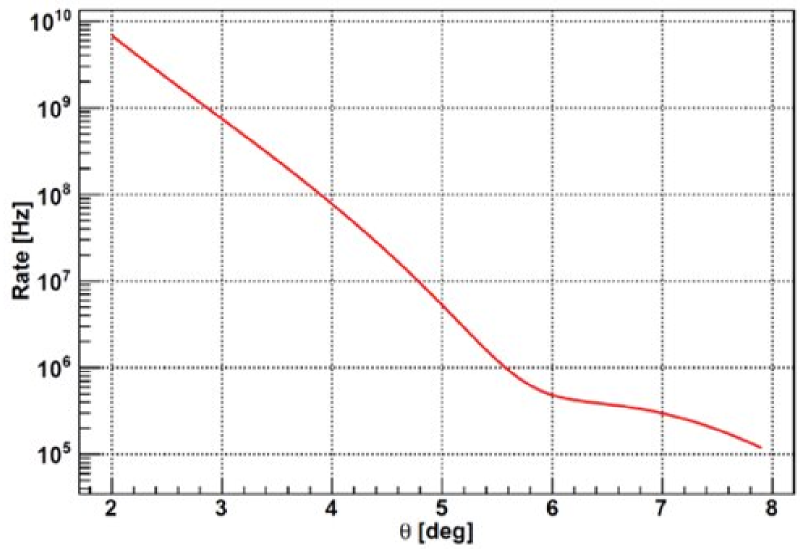

Fig. 3. Measured asymmetry vs. scattering angle. The measured asymmetry vs. scattering angle for a 100 μA beam at 2.2 GeV. The asymmetry is averaged over the acceptance of the HRS and septum.

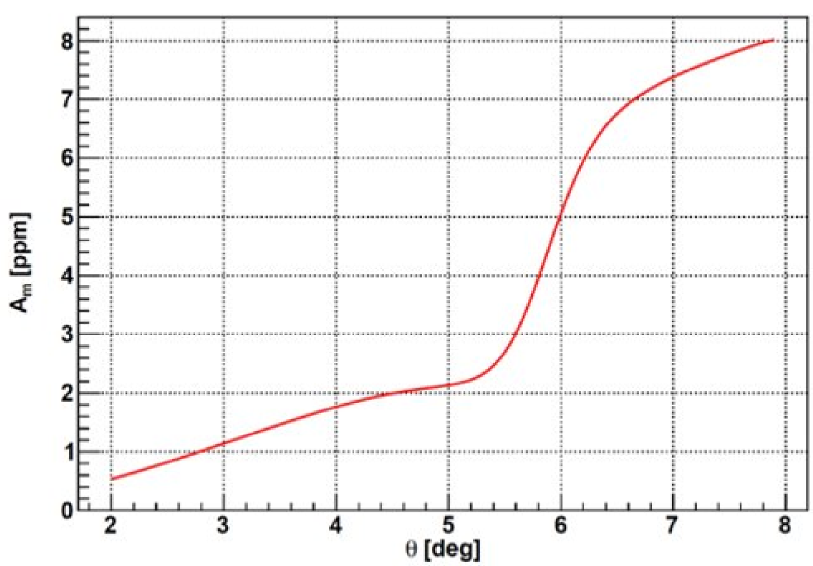

The optimum kinematics for the experiment are chosen based on experimental parameters which maximize the figure-of-merit (FOM), defined as

$$FOM = Rate \times A_{PV}^2 \times \epsilon^2 \quad [7]. \tag{4}$$

ϵ takes into consideration the sensitivity of A_{PV} to a small change in R_n,

$$\epsilon = \frac{R_n}{A_{PV}} \frac{dA_{PV}}{dR_n}, \tag{5}$$

where dR_n denotes the change in R_n and dA_{PV} is the corresponding change in A_{PV} [3]. The sensitivity term in the FOM equation ensures that by maximizing the FOM the error in R_n is effectively minimized [7]. Fig.4. shows the θ dependence of the absolute error in the $R_n(^{48}\text{Ca})$ measurement for a 100 μA beam at 2.2 GeV. This figure was also provided by Dr. Mammei. I use this in order to demonstrate the very forward angles which are required to minimize the error in the measurement of R_n.

Fig. 4. Error in R_n vs. scattering angle. The absolute error in the R_n measurement, averaged over the acceptance of the HRS and septum, vs. scattering angle for a 100 μA beam at 2.2 GeV. With an assumed systematic error of 1.8% there is a slight change in the FOM calculation (solid red line).

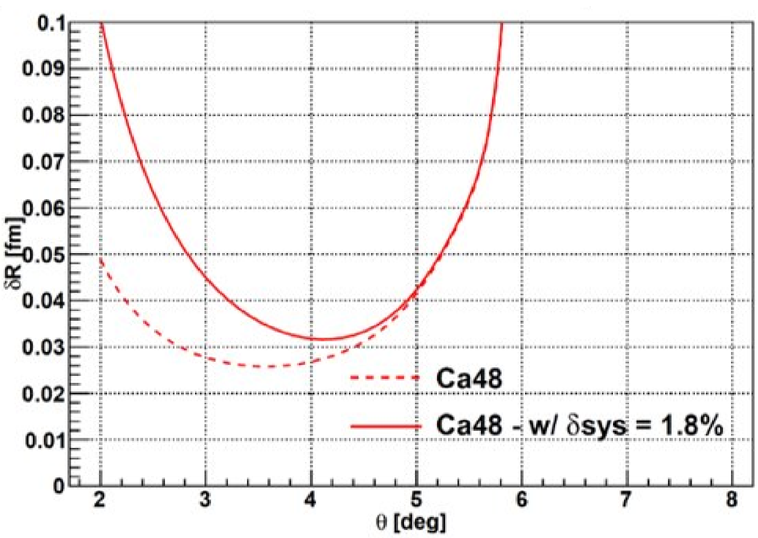

B. Thesis Subject and Contents

1) Magnetic Saturation in the Septum Magnet: As I recently touched on, the error in the R_n measurement is minimized by very forward scattering angles. Since the minimum acceptance angle of the HRS is 12.5^o, a pair of bending magnets upstream of the HRS are necessary to achieve the small scattering angle in both detector arms. The septum magnet had been used for this purpose during the running of PREX-1 at a nominal current of 377 A, well within the linear range of its operation. However, the magnet field response becomes non-linear at a characteristic current as magnetic saturation sets-in in the iron material. This is of particular concern at the CREX kinematics because while the beam energy is more than double that of PREX-1 and PREX-2 the optimum scattering angle remains similarly small. As a consequence the septum magnet must be operated at an aggressively high current at which point magnetic saturation in the return yoke and beam pipe shield is expected.

To reach the minimum acceptance angle of the HRS at CREX kinematics, the septum magnet needs to bend the scattered electron beam from around 3^o to 12.5^o which corresponds to a field integral of 1.21 Tm. First, it was necessary to confirm that the septum magnet could reach the field strength required for such a task. Inside the magnet gap the field strength drops below linear as magnetic saturation sets-in and depending on the extent of the saturation, it may not be possible to reach the field strength that is required for CREX within the operational range of the magnet. In addition, magnetic saturation throughout the iron material is non-uniform, therefore field saturation in the magnet gap is position dependent. It becomes necessary, then, to characterize the field response at a few locations within the magnet gap to better understand the effect that saturation has on the field strength and homogeneity.

The pipe that carries the high-energy beam toward the beam dump is passed through the septum magnet, which is equipped with a steel magnetic shield through its centre. The shield was designed to reduce the stray field lines at the beam pipe that would cause vertical and horizontal deflections of the beam. This is important to prevent particles from impinging on the beam pipe and contributing to radiation in the hall. Unfortunately, magnetic saturation in the original shield at the PREX kinematics rendered the shield insufficient at keeping radiation down and was one of the causes of low running efficiency during the running of PREX-1. This effect is expected to be greater at the much larger septum current that is required for CREX but should be confirmed by simulations. Further, a new beam pipe shield which is extended at the upstream and downstream edges of the magnet needs to be simulated to confirm the reduction of the fringe field and the total field integral, through the septum magnet, inside the beam pipe.

2) Data Acquisition by FEA Simulation: The field data were acquired from finite element analysis (FEA) simulations of the magnetic system. Such a numerical technique requires a description of the system geometry (the domain) and the discrete mesh that approximates the domain on which the PDE is defined. The mesh is composed of finite elements, which have basic geometries, and nodes. Each element corresponds to local shape functions which are combined linearly to approximate the solution defined on the element's domain. The element solutions are coupled by the condition of solution continuity at the inter-element boundaries. Given this, a global system of linear equations may be constructed. In the case of a magnetostatic system, the magnetic scalar potential is approximated at the mesh nodes and the solution is interpolated by the local shape functions at those positions between the nodes. In Section A. of Chapter II. I provide a detailed description of the septum magnet and present the two magnetic scalar potential formalisms used. I follow this with a section on the finite element method (Section B. of the same chapter).

Opera Vector Fields provides a suite of software packages for 3-d modeling, Tosca magnetostatic analysis, and post-processing of electromagnetic (EM) fields. To prepare the magnetic system for the FEA analysis program, I used the 3-d geometric modeler package to build a model of the septum magnet and set the finite element mesh and analysis parameters. The magnet coils were modeled by a stack of conductors, for which the current density could be varied. I tuned the mesh parameters inside the magnet air gaps and iron components to achieve a good field quality in these regions. Once the magnetic system is set up, a model data set may be generated and the analysis program can be run. Since the model equation is non-linear, Tosca performs Newton-Raphson iterations until the solution converges. The solved simulation gets written to an Opera 3-d database file, which can be accessed and interpreted by the post-processor software package. Section A. of Chapter III. contains details of this entire procedure.

3) Field Analysis and Investigation: The two regions of interest in the septum magnet are the magnet gap, where the scattered electron beam is deflected, and the beam pipe gap, which is surrounded by the magnetic shield. In Section B. of Chapter III. I cover the procedure for analyzing the field in both regions. This primarily concerns the transverse field homogeneity, path integration of the field through the magnet, and the characterization of the non-linear field response.

To observe the field response of the magnet, a new field simulation was created for a number of different current density settings. I used the post-processor to generate field maps for each simulation and used a python script to aggregate and organize the data into 15 (I_i, B_i) data pairs at a number of locations within the magnet gap. I used least-squares linear regression to fit the data in the linear region of the field response and extrapolated into the high-current region in order to measure the field drop-off. These results are presented in Section A. of Chapter IV..

The vertical field integral through the length of the magnet gap directly corresponds to the deflection angle of the scattered electron beam as it travels through the septum magnet. To meet the HRS acceptance for $\theta = 3^o$ at the CREX beam energy (2.2 GeV) the requisite septum field integral is 1.21 Tm. I used the Tosca simulations to determine the septum current setting suitable for CREX. Further, I examined the variation of the field integral within the acceptance zone of the magnet gap. The results of this analysis are presented in the first part of Section B. of Chapter IV..

Chapter IV. ends with the results of the fringe field minimization study. I used the Tosca simulations to confirm magnetic saturation in the original shield at high-current and to examine the effects this has on the field inside the beam pipe. These results were used as a point of comparison for a model of the septum magnet with shield extensions at the upstream and downstream edges. I examined the field strength profile along the length of the magnet for both models. Additionally, I evaluated the field integral inside the beam pipe, because this indicates the deflecting potential of the stray field on the high-energy beam. I conclude the thesis in Chapter V..

II. Theory

The present chapter is separated into two sections. In the first section, I will describe the function of the septum magnet in the beam transport system. I will provide the equation which governs the particle motion inside of a vertical dipole magnet and show how the steering of the electrons is dependent on the physical parameters of the particle and the magnet. This will be followed by a description of the septum magnet that will illustrate the function of the major components, setup the geometry and define important regions of the magnet. I will close off this section by presenting the magnetic scalar potential formulation that is used by the Tosca software. This allows for two representations of the magnetic field to be used on separate regions of the domain, distinguished by the presence or absence of free electric currents, and coupled at the interface by field continuity requirements. In the second section of this chapter, I will describe the numerical methods that form the basis of the Tosca algorithm which solves for the magnetic scalar potential of the system.

A. The Magnetostatic System

1) Particle Steering in the Magnet Gap: At CEBAF, an electron beam is longitudinally polarized and accelerated to near the speed of light. The relativistic beam is then injected into the experimental hall and transported by a system of magnets to the interaction point inside the scattering chamber. Downstream, the septum magnet bends the forward scattered electrons horizontally to reach the lowest acceptance angle of the HRS. This is achieved with a static dipole magnetic flux, $\vec{B}$, which changes the direction of the particle momentum, $\vec{p}$. The magnet is oriented so that its length, L, is along the z-axis - in the direction of beam propagation - and the direction of the flux is vertical, $\vec{B} = \pm B_y\hat{y}$, chosen to be in the $+\hat{y}$ direction in the left dipole and $-\hat{y}$ in the right. Fig.5. provides a schematic of a dipole magnet cross-section for reference.

Fig. 5. Cross-section of a vertical dipole magnet. A front perspective of a single dipole magnet with a transverse-plane cut. Shown are the ideal (uniform) magnetic flux lines inside the dipole magnet gap. The cross-sectional area of the conductor is indicated by A. Also shown are the coil turns and current direction in the conductors.

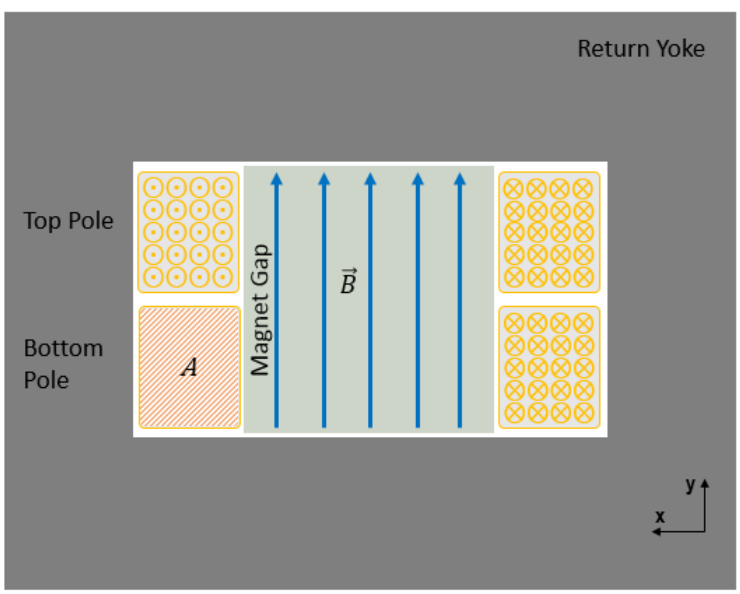

Electron motion through the magnet is governed by the Lorentz force equation

$$\vec{F} = q\vec{v} \times \vec{B}, \tag{6}$$

where q and $\vec{v}$ are the electron charge and velocity, respectively. It is convenient to write $\vec{v}$ in terms of the velocity components that are parallel ($v_y\hat{y}$) and perpendicular ($\vec{v}_\perp$) to the direction of the magnetic flux, $\vec{v} = v_y\hat{y} + \vec{v}_\perp$. Then (6) becomes

$$\vec{F} = \pm B_y q(\vec{v}_\perp \times \hat{y}). \tag{7}$$

In the plane normal to the magnetic flux the electron motion is circular and the path through the magnet is an arc with radius R, referred to as the bending radius. Balancing of the radial force and centripetal acceleration relates the bending radius to the physical parameters of the magnet and particle [8],

$$\frac{\gamma m_0 v_\perp^2}{R} = B_y q v_\perp. \tag{8}$$

m_0 is the electron rest mass and γ is the Lorentz factor.

Assuming that v_y is much smaller than $v_\perp$ so that $v_\perp \approx v$, the relation $p = \gamma m_0 v = \frac{\beta E}{c}$ can be used to express (8) in terms of the particle energy

$$\frac{1}{R} = 0.2998\frac{B_y}{\beta E}, \tag{9}$$

for R in metres, B_y in Tesla, and the total particle energy in GeV [9]. β is defined as the ratio of the particle velocity to the speed of light and is approximately 1 for relativistic particles.

The particle emerges from the dipole deflected from it's initial trajectory by an angle θ, given by

$$\theta = \int \frac{1}{R} ds = \frac{1}{3.336E}\int B_y ds, \tag{10}$$

where ds is the path length associated with the turn angle $d\theta$ [10], [9].

2) Iron-Dominated Dipole Magnet Pair: The septum magnet is composed of two dipole magnets, referred to as the left and right dipoles. A physical septum - the beam pipe shield - at the centre separates the high-field regions from the zero-field region and a return yoke encases all the internal components. For reference see Fig.6.. The return yoke and beam pipe shield are both manufactured from low-carbon steel material. It is a soft ferromagnet defined by a large and non-constant magnetic permeability, $\mu = \mu(H)$. When magnetized by the coil field, this induces a magnetic flux (or, induction) $\vec{B}$ that is related to the magnetic field by the equation

$$\vec{B} = \mu(H)\vec{H}. \tag{11}$$

Fig. 6. Photos of the assembled septum yoke and coils. Front (left image) and side (right image) view of the septum magnet return yoke and coils. Centre shield is not shown.

The net effect of the magnetized iron yoke is the strengthening of the magnetic flux density inside the dipole magnet gaps (the high-field region) by a few orders of magnitude. This is attained by redirection of the flux inside the yoke. The 2D colour vector maps in Fig.7. provide a visual of this effect for the septum magnet. Similarly, the magnetized shield contains and redirects the stray magnetic flux away from the region where the beam pipe is located. The shield was designed with the purpose of minimizing deflection of the high energy particles as they are transported through the magnet and toward the beam dump. I mention these effects with the following caveat, saturation of $\mu(H)$ in the iron components results in nonlinear effects on the magnetic flux density and uniformity.

Fig. 7. 2D vector maps of the septum magnet. Front perspective of the left dipole, as modelled in Opera, overlaid with a 2D color vector map of $\vec{B}$. Shown are two images: left dipole coils (left image) and the same coils with the iron components (right image). Note that the iron components are visible for the top half of the magnet only.

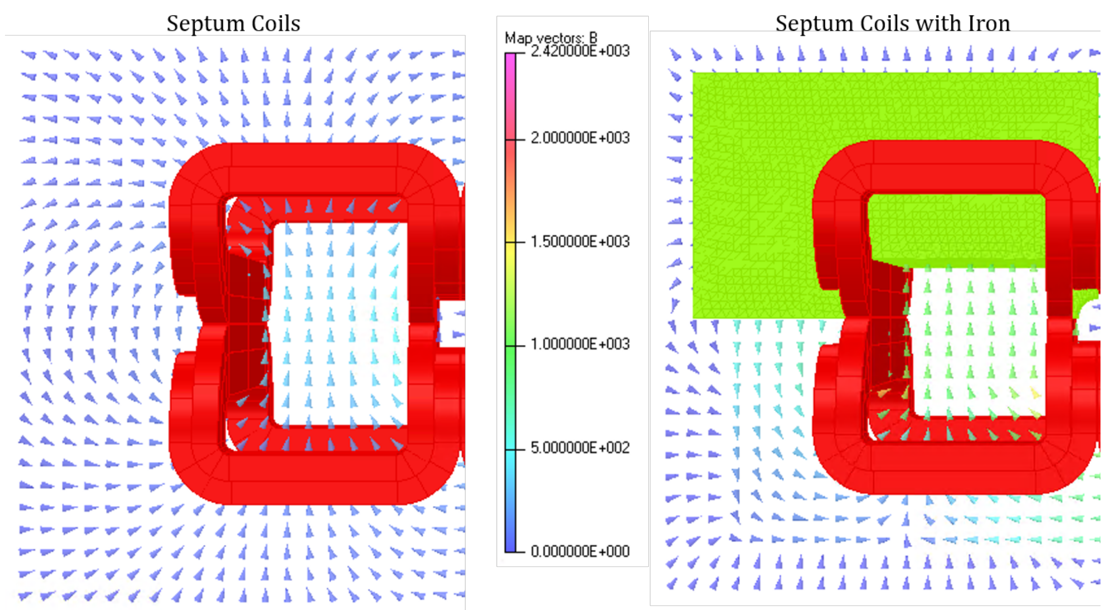

The ferromagnetic response to an external magnetic field (expressed in (11)) is a bulk property measured empirically by tracing a hysteresis loop. The data may be presented as a BH curve, where the magnetic flux induced by an external $\vec{H}$ field that magnetizes the material is plotted against H (see Fig.8.). Such a plot shows the saturation point of the magnetic permeability for $\vec{H}$ applied in one direction and in the opposite (negative) direction.

Fig. 8. BH curve of 1010 steel.

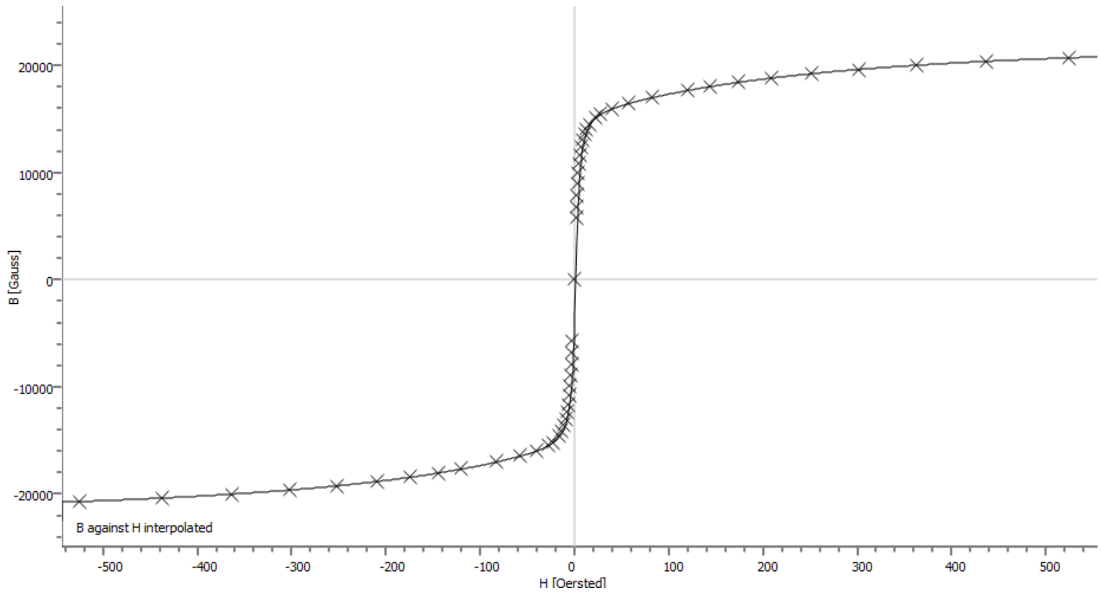

Each magnet pole is constructed of tightly-wound coils with a total number of turns, N_t. The strength scales linearly by the total number of turns, measured as $N_t I_{ps}$ amp-turns, for a power supply current I_{ps}. I approximate the magnet pole as a conductor with a cross-sectional area A and a current density J that is related to the coil parameters by the equation,

$$J = N_t I_{ps}/A. \tag{12}$$

The conductor field at an observation point $\vec{r}$ is given by the Biot-Savart law

$$\vec{H}(\vec{r}) = \int_{\Omega'} \frac{\vec{J}(\vec{r'}) \times (\vec{r} - \vec{r'})}{|\vec{r} - \vec{r'}|^3} d\Omega', \tag{13}$$

integrated over the conductor volume Ω'. This accounts for the source field of the septum magnet, controlled by the input parameter I_{ps}, and is what excites the iron-dominated components.

3) Magnetic Scalar Potentials: The septum magnet field is numerically solved using Tosca Finite Element Analysis (FEA) software. The Tosca algorithm uses a formalism based on two magnetic scalar potentials separately defined in different regions of the domain. On the region of the domain that is free from electric currents ($J = 0$), denoted by Ω_t, the total magnetic field can be represented as the gradient of a scalar potential [11],

$$\vec{H}(\vec{r}) = -\nabla\Phi_t(\vec{r}) \quad : \vec{r} \in \Omega_t. \tag{14}$$

Φ_t is referred to as the total scalar potential. For the region that contains electric currents, denoted by Ω_r, the total magnetic field can be separated into two components [11],

$$\vec{H}(\vec{r}) = \vec{H}_m(\vec{r}) + \vec{H}_s(\vec{r}) = -\nabla\Phi_r(\vec{r}) + \int_{\Omega'} \frac{\vec{J}(\vec{r'}) \times (\vec{r} - \vec{r'})}{|\vec{r} - \vec{r'}|^3} d\Omega' \quad : \vec{r} \in \Omega_r \tag{15}$$

where $\vec{H}_m$ is referred to as the reduced field and Φ_r is the reduced scalar potential. Note that $\vec{H}_s$ is the coil field (see (13) for reference).

Both representations of the magnetic field satisfy Maxwell's equation

$$\nabla \times \vec{H} = \vec{J}, \tag{16}$$

on their respective sub-domain [12]. Since the divergence of the magnetic flux is always zero, the governing equations are therefore,

$$\nabla \cdot \mu\nabla\Phi_t(\vec{r}) = 0 \quad : \vec{r} \in \Omega_t \tag{17a}$$

$$\nabla \cdot \mu\nabla\Phi_r(\vec{r}) - \nabla \cdot \mu\vec{H}_s(\vec{r}) = 0 \quad : \vec{r} \in \Omega_r \tag{17b}$$

The two representations of the magnetic field are coupled by imposing continuity conditions at the interface of Ω_t and Ω_r. These conditions are that the normal component of $\vec{B}$ and the tangential component of $\vec{H}$ are continuous [11], [12].

For the septum magnet, the coils are not situated inside the iron material which makes it possible to construct a reduced potential region outside of the iron components. In this case, the reduced potential region would contain the dipole coils in a region of air. The permeability in (17b) is the magnetic permeability of air which is approximately that of free space. In the total potential regions that contain the iron components, the magnetic permeability is a variable scalar, since we assume that the material is isotropic, and is given by the BH data of 1010 steel (see Fig.8.). $\vec{H}_s$ is a known functional and can be directly integrated.

Equations (17a) and (17b) are a form of Poisson's equation,

$$-\nabla \cdot \mu \nabla \phi(\vec{r}) = s(\vec{r}) \quad : \vec{r} \in \Omega, \tag{18}$$

where $\phi(\vec{r})$ denotes the scalar potential, μ is the permeability, and $s(\vec{r})$ denotes the source function, defined on the domain, Ω. The Tosca algorithm solves this equation by defining local approximations of the solution on discrete volume elements of the domain. This is accomplished by using the weighted residual method with a choice of Galerkin weighting functions to solve for the scalar potential values at the nodes of the finite element mesh. These steps will be described in more detail in the next section of this chapter.

B. Numerical Methods of Solution Approximation

1) Domain Discretisation: The finite-element method (FEM) is a technique used to numerically solve a PDE defined on a complex domain. This works on the basis of a piece-wise application of a variational method of solution approximation [13]. The procedure starts with the generation of a finite element mesh over the entire domain, Ω. Ω is divided into a finite number of discrete elements using geometrically simple volumes labeled 1 to D. The points of element intersection are called the global nodes, or inter-element boundaries. These points are labeled 1 to N. Together, the labeled nodes and elements make up the finite-element mesh. Once the mesh is generated, local approximations of the solution are defined on each element domain. In Fig.9. the finite-element mesh approximates an arbitrary area bordered by a line. The mesh is composed of triangular elements Ω_e that have three local nodes each. This is an example of a surface mesh, however, the concept can be extended to three dimensions.

Fig. 9. A finite-element mesh on an arbitrary domain. A representation of a finite-element mesh approximating an arbitrary domain Ω.

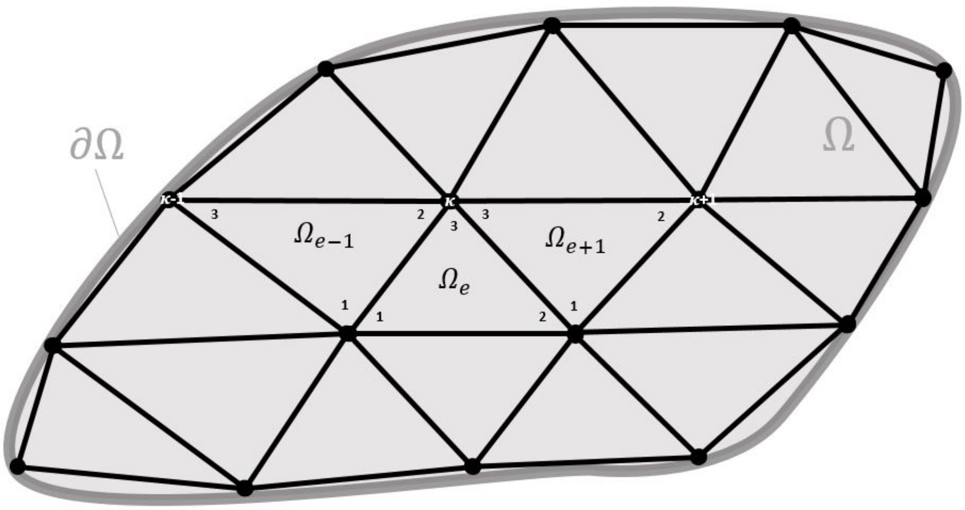

2) Local Solution Approximation: The local solution $\phi^e(\vec{r})$ on the element domain Ω_e is defined by a linear combination of approximation functions $N_j^e(\vec{r})$,

$$\phi^e(\vec{r}) = \sum_{j=1}^{M} \phi_j^e N_j^e(\vec{r}). \tag{19}$$

The summation in (19) is over the nodes of element e, locally numbered 1 to M. $N_j^e(\vec{r})$ are the nodal shape functions, each associated with a particular node in the element. These are locally defined polynomials with the following properties,

$$N_j^e(\vec{r}_i) = \delta_{ji} \tag{20a}$$

$$\sum_{j=1}^{M} N_j^e(\vec{r}) = 1 \tag{20b}$$

where r_i denotes the coordinate of node i and δ_{ji} is the Kronecker delta [13]. Additionally, N_j^e are zero outside of the element e. The local solution is defined such that at node j it is equal to the nodal parameter ϕ_j^e and at points on the element domain that are not nodes the solution is interpolated.

To determine the nodal parameters, the method of weighted residuals is used, which requires a choice of weighting function. In the Tosca algorithm, the Galerkin weighting function is used [11], $W^e(\vec{r}) = \sum_{i=1}^{M} N_i^e(\vec{r})$ from the same set of functions that approximate $\phi^e(\vec{r})$. Additionally, a set of residual functions are defined for each element solution,

$$R^e \equiv -\nabla \cdot \mu \nabla \phi^e(\vec{r}) - s^e(\vec{r}) \neq 0, \tag{21}$$

R^e is referred to as the residual function of element e and is a measure of error in $\phi^e(r')$. Next the parameters of (19) are determined by integrating the product of the weighting and residual functions over the element domain and setting to zero,

$$0 = \int_{\Omega_e} W^e(\vec{r}) \left(-\nabla \cdot \mu \nabla \phi^e(\vec{r}) - s^e(\vec{r})\right) d\Omega_e. \tag{22}$$

The variational (or, weak) form of (22) is obtained by applying Green's first identity, which gives the equation

$$\int_{\Omega_e} \nabla W^e(\vec{r}) \cdot \mu \nabla \phi^e(\vec{r}) d\Omega_e = \int_{\Omega_e} W^e(\vec{r}) s^e(\vec{r}) d\Omega_e + \oint_{\Gamma_e} W^e(\vec{r}) \left(\mu \nabla \phi^e(\vec{r}) \cdot \hat{n}\right) d\Gamma_e. \tag{23}$$

Here, Γ_e is the boundary of Ω_e and $\hat{n}$ is the unit vector outward normal to the infinitesimal surface element. By casting the equation into the weak form, the differentiation is distributed among ϕ^e and W^e so that these functions are each required to be only once differentiable on the element domain [13]. The left-hand side of (23) can be rewritten as

$$\sum_{i=1}^{M} \sum_{j=1}^{M} \phi_j^e \int_{\Omega_e} d\Omega_e \nabla N_i^e(\vec{r}) \cdot \mu \nabla N_j^e(\vec{r}), \tag{24}$$

and the right-hand side as

$$\sum_{i=1}^{M} \left[\int_{\Omega_e} d\Omega_e N_i^e(\vec{r}) s^e(\vec{r}) + \oint_{\Gamma_e} d\Gamma_e N_i^e(\vec{r}) q_n \right], \tag{25}$$

where $q_n = \mu \nabla \phi^e(\vec{r}) \cdot \hat{n}$ [13]. What we have is a local system of linear equations, which in matrix form is

$$K^e \Phi^e = S^e. \tag{26}$$

K^e is the element stiffness matrix $(M \times M)$, S^e is the M-d vector of known functions (which include the surface integral term), and Φ^e is the M-d vector of the nodal parameters ϕ_j^e.

3) Global Matrix and Solution Iteration: The global matrix equation of the model is constructed by assembling the local equations, (26), of all the elements in the mesh. This requires knowledge of the correspondence between the global and local nodes and imposing solution continuity at the inter-element boundaries. The form of the global matrix equation is

$$K\Phi = S. \tag{27}$$

Φ is the N-d vector that contains the global nodal parameters ϕ_κ, K is the $N \times N$ global stiffness matrix and S is the N-d vector of the global source functions. The global stiffness matrix is constructed out of the element stiffness matrices K^e. Likewise, S is made up of S^e.

Global to local node correspondence information is contained in the connectivity matrix, C, whose element C_{ej} is equal to the global node number that corresponds to local node j of element e. For example, suppose that global node κ is an intersection point of element e at local node j and element $e+1$ at local node j'. See Fig.10. for reference. Then the (e, j) and $(e+1, j')$ locations of the connectivity matrix both have κ as the entry. Additonally, for the solution to be continuous at the node κ it is required that $\phi_j^e = \phi_\kappa = \phi_{j'}^{e+1}$.

Fig. 10. Global to local node correspondence. Global node κ at the intersection of local node j of element e and local node j' of element $e+1$. In this particular example the local nodes are labeled counterclockwise. c is an arbitrary positive integer.

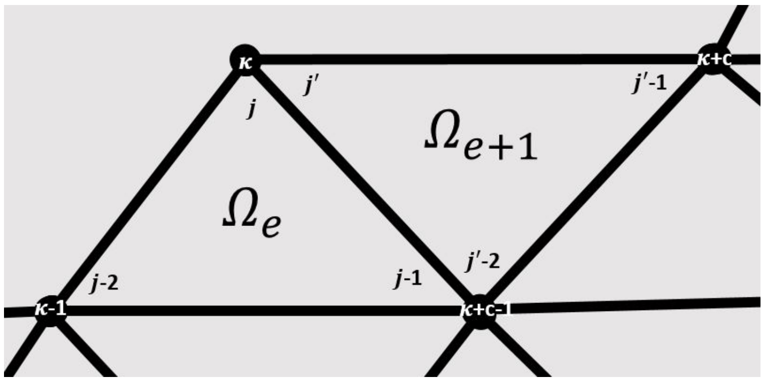

A diagonal element of the global stiffness matrix K_{ii} $(i = 1, 2, ..., N)$ is equal to the sum of the corresponding (local node) diagonal element of K^e for those finite elements that intersect at global node i. For example, in Fig.10. the corresponding diagonal element of K at node κ is given by $K_{\kappa\kappa} = K^e_{jj} + K^{e+1}_{j'j'}$. The off-diagonal (or, cross-term) elements of the global stiffness matrix $K_{ii'}$ $(i \neq i'$ and $i, i' = 1, 2, ..., N)$ express the correspondence between two global nodes anywhere in the mesh. This term is zero for all nodal pairs which are not part of the same finite element.

The global matrix equation is solved by determining the matrix inverse of K and computing the following matrix product,

$$\Phi = K^{-1}S. \tag{28}$$

Because the model equation is non-linear, the solution needs to be iterated until it converges. Tosca does this using a Newton-Raphson method [11]. For a model solution of the n^{th} iteration, Φ_n, two matrices are defined: the residual,

$$R_n = K_n\Phi_n - S_n, \tag{29}$$

and the Jacobian,

$$J_n = \frac{\partial R_n}{\partial \Phi_n}. \tag{30}$$

These give rise to a new solution, given by

$$\Phi_{n+1} = \Phi_n - J_n^{-1} R_n. \tag{31}$$

III. Procedure

In the first section of this chapter, I detail the procedure for preparing the 3D model of the septum magnet and the finite element mesh in order to run the Tosca FEA analysis program. In this process I place the model within a global Cartesian coordinate system and define its dimensions. I describe the subdivision of the air blocks, which allow a greater flexibility in tuning the mesh control parameters throughout the model, and then detail the mesh control settings assigned to the individual bodies that make up the model. I conclude this section with descriptions of the material properties, scalar potential settings, boundary conditions, and element type, all of which are parameters required for the analysis program.

The second section of this chapter concerns the post-processing of the field simulations and the data analysis procedures I used. It is structured similarly to the presentation of results in the chapter that follows. I define the local coordinate systems in the two regions of interest in this study: the magnet gap and the beam pipe gap. Since there is symmetry of the left and right dipoles, I analyzed the field of the left magnet only. I detail the procedure to generate the field data tables and the aggregate data sets using the Opera 3D post-processor. Analyses in both regions concern the transverse field homogeneity, path integration of the field through the magnet, and the non-linearity of the field response to conductor current.

A. FEA Simulations of the Septum Magnet

1) Geometric 3D Model: I modelled the septum magnet using the Opera-3d modeller. The model is based on the magnet in the 2-coil configuration, a return yoke with shims, and a symmetric beam pipe shield that extends from the upstream edge to the downstream edge of the yoke. I positioned the magnet so that it is centered at the origin of the global coordinate system and its longitudinal dimension is on the z-axis. A single magnet pole is composed of two bedstead conductors (a standard conductor geometry in the modeller). The more massive conductor, coil 2, is positioned on top of the smaller conductor, coil 1, to form the pole. See Fig.11. for its geometry. I created the rest of the poles by reflecting the single pole in the xz and yz planes for a total of four magnet poles. These are shown in Fig.13. with the iron components. The conductors are the only entities of the model that are not part of the finite element mesh.

Fig. 11. Magnet pole geometry. A magnet pole composed of two stacked bedstead coils.

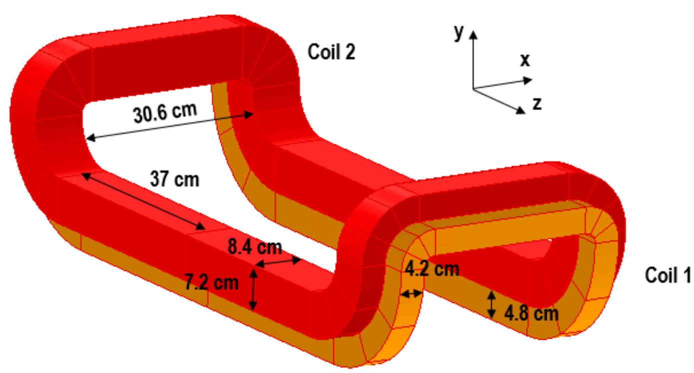

To generate the rest of the model (the iron and air components) I used primitive geometries such as blocks and cylinders and performed boolean operations on them. The return yoke is composed of a number of blocks, which were positioned to form the shape of the yoke and then merged together to create a single body. To create the beam pipe shield, I generated a block and cylinder of the same length, positioned the cylinder within the block, and deleted the intersecting volume from the block before deleting the cylinder. These iron components of the model are shown in Fig.12..

Fig. 12. Iron components of the model. The geometry of the return yoke with shims and of the symmetric short shield created in the modeller.

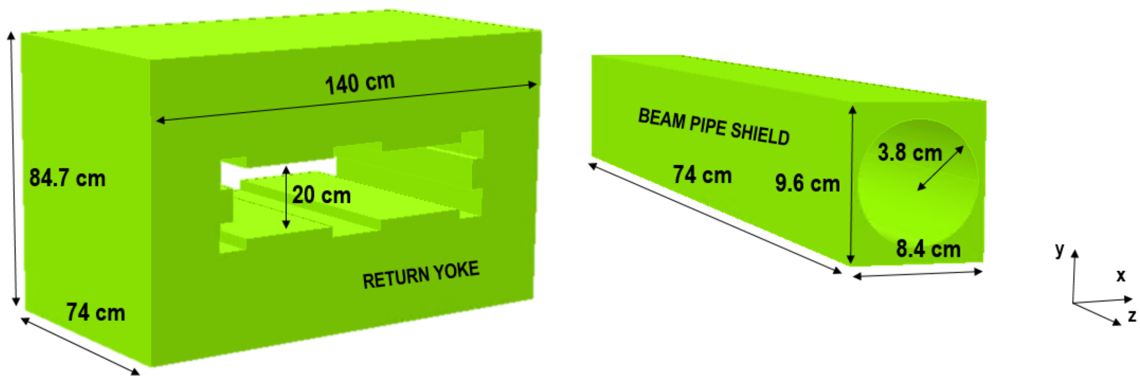

In order to generate the finite element mesh, the model must also include bodies of air. The blocks of air that run within the magnet, such as in the left and right magnet gaps and within the beam pipe shield, extend from z=-100 cm to z=+100 cm. This covers the spatial regions where field accuracy is required for the purpose of the study. I created the external model air with three nested blocks, centered at the origin. These encompass the septum magnet and internal blocks of air. The outermost air shell bounds the model with dimensions 620 × 400 × 800 cm^2. These are shown in Fig.13. with the rest of the model. The **BACKGROUND** command creates a background space and defines the model symmetry and boundary conditions. I set the size of this space to three times the size of the outermost air block. I discuss the symmetry and boundary conditions in the following sections. The final step before generating the finite-element mesh is to merge all the bodies into a single, topologically-valid structure.

Fig. 13. Air components of the model. The internal (left) and external (right) air blocks of the model. Also shown are the coils and iron components.

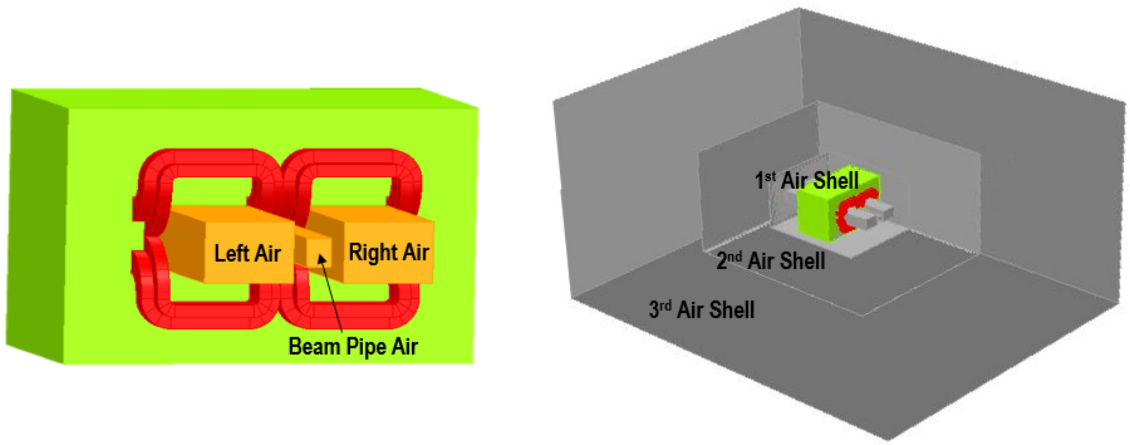

2) Finite Element Mesh: The septum magnet model was meshed in the modeller via two commands that control and execute the construction of the surface and volume meshes. The process begins with a surface mesh that is sequentially generated on every cell face. Once every surface of the model has been sub-divided the volume of each cell is filled, in sequence, with discrete volume elements. Since I set model reflections in the xz and yz coordinate planes the finite element mesh was generated for a single quadrant of the model. See Fig.14. for reference.

Fig. 14. Model symmetry. The xz and yz coordinate planes where the model is reflected.

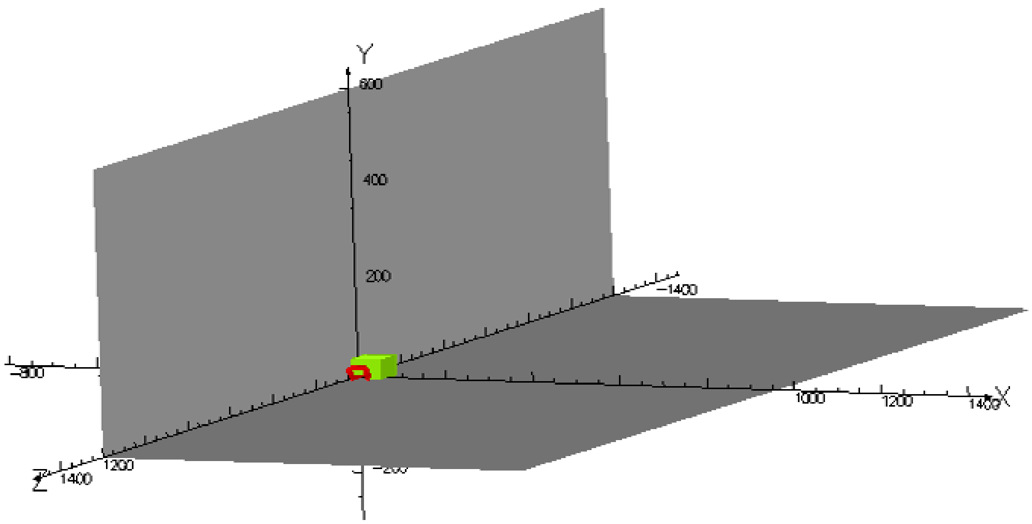

A basic source of error in the model solution is introduced in the approximation of the model domain by finite elements. As the mesh is refined it better approximates the domain and therefore minimizes this boundary error in the solution. At the same time, because the field studies presented in this thesis are entirely contained within the first air shell of the model the approximation of the domain far outside of that is not crucial. The regions of the model where an accurate field solution is required is in the cells of the return yoke, shield, and inner air volumes. I refined the mesh in those regions by tuning the mesh control parameters, defined in Table I, that are specified in the cell data of each body.

Table I

Mesh Control Parameter Definitions

SIZE	Element size
NORMALTOL	Normal angle between facets
SURFACETOL	Deviation from surface
TOLERANCE	Point coincidence
TYPE	Element shape

Mesh granularity on a cell face is dictated by the SIZE parameter, defined as the maximum element size allowed in the mesh of that cell. To control the fit of the surface mesh on a curved cell face, which is present in beam pipe shield, two tolerance parameters are applied to those cells, NORMALTOL and SURFACETOL. The former sets the maximum allowable angle, in degrees, between the normal vectors of neighboring surface elements. The latter parameter constrains the absolute distance from the element centroid to the model surface. Table II contains the tuned values that I assigned to these mesh control parameters for each model entity. For both the surface and volume mesh, I set the the tolerance for point coincidence to 1.0E-08 cm and the element shape to tetrahedral.

Table II

Mesh Control Parameter Settings For Model Bodies

Body	Yoke	Shield	Pipe Air	Gap Air	1st, 2nd, 3rd Air Shell
SIZE	2	1	1	2	2, 4, 16
NORMALTOL	na	5°	5°	na	na
SURFACETOL	na	0.1 cm	0.1 cm	na	na

3) Tosca Magnetic Analysis: The cell properties that directly pertain to the FEA simulation are the scalar potential, material characteristics, and element type. The analysis algorithm is based on reduced and total scalar potential formulations. For volumes that contain currents the potential was set to “reduced” and for all others it was set to “total”. During construction of the model geometry the material label “Iron” was assigned to the cells of the return yoke and beam pipe shield. Associated with that label is the material permeability, set to non-linear and isotropic, and the BH data, which was loaded from a file of the BH curve of 1010 low-carbon steel. In the air volumes the cells were assigned the program’s default label, “Air”. The type of finite element that is created in a cell volume may be linear or quadratic. An element type has a characteristic number of local nodes and associated nodal shape functions. This property was set to quadratic for all cells in the model; a quadratic tetradehral has four local nodes, one at each vertex, plus six nodes placed at points between the vertices [11].

The far-field boundary, shown in Fig.15., was extended outwards via the background space to mitigate the truncation effect in the regions of interest. Truncation of the field solution occurs when an infinite domain is approximated by a finite volume [11]. The dimensions of the background space were set to three times those of the outermost block of air and the model was reduced to one quadrant based on symmetry. A derivative boundary condition was applied to the outer surface, $\frac{\partial \Phi}{\partial n} = 0$ (Φ refers to the magnetic scalar potential that is just interior to the open boundary). To impose the field symmetry the potential boundary condition $\Phi = 0$ was applied to the xz and yz coordinate planes where the model is reflected (Fig.14.).

Fig. 15. Model far-field boundary. The external surface of the model where the far-field boundary condition is imposed.

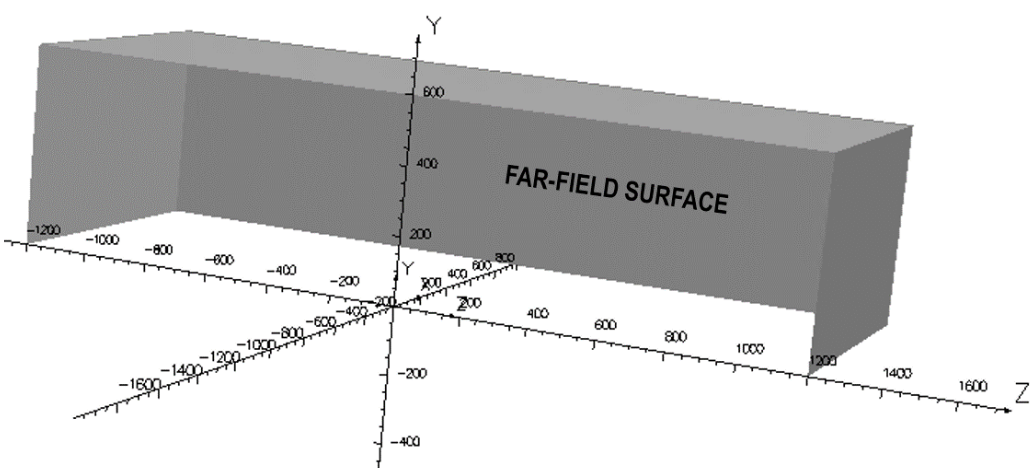

The simulation was solved with the Tosca magnetic analysis program. Due to the presence of iron components in the model the program was configured to perform non-linear iterations of the solution using the Newton-Raphson non-linear update method. By this method a residual (29) and Jacobian (30) are updated each iteration and used to solve for the new solution. The program determines that the solution has converged using either of the following criteria [11],

a) The maximum and RMS solution changes are less than the convergence tolerance

b) The norm of the residual is less than 1% of the convergence tolerance squared.

The solution convergence tolerance is the default, 0.001. The solved simulation was written to a Opera 3-d database file, which can be opened and read by the post-processor.

B. Post-Processing and Analysis

1) Vertical Field Variation in the Magnet Gap: In the high-field region of the septum magnet B_y is the dominant field component. It provides the horizontal deflection to the scattered electrons that pass through the gap. A local coordinate system is used in this region, which transforms from the GCS in the following way,

$$\tilde{x} = x - 23.8cm, \quad \tilde{y} = y, \quad \tilde{z} = z. \tag{32}$$

At the centre line of the magnet gap, the central dipole field is entirely vertical, $\vec{B}_0(\tilde{z}) = B_{y0}(\tilde{z})\hat{y}$. This is in general not true of the dipole field $\vec{B}(\vec{\tilde{r}})$ at positions $\tilde{x} > 0$ cm and $\tilde{y} > 0$ cm. The outward changes of B_y from the centre of the gap is measured by the field variation - denoted by $B_y var$ - as a function of position in the dipole. At some constant position inside the magnet $\tilde{z} = z_0$, $B_y var$ is computed from the equation

$$B_y var(\tilde{x}, \tilde{y}) = \frac{B_y(\tilde{x}, \tilde{y}, z_0) - B_y(0, 0, z_0)}{B_y(0, 0, z_0)}. \tag{33}$$

The vertical field variation is measured as a fraction of B_y at the reference point $p_r(z_0)$ located on the centre line, or, $B_0(z_0)$.

The transverse cross-section defined within the perimeter of the magnet gap has dimensions $h = 20$ cm and $w = 30$ cm. Using the Opera 3D post-processor, a two dimensional grid of B_y, evaluated at $\tilde{z} = z_0$, is generated and output as a table file. Each point on the grid refers to a position on the transverse cross-section. Due to the field symmetry at the xz global coordinate plane, B_y is evaluated for the top half of the transverse slice only. The two dimensional grid contains 31 points along the horizontal axis, equally spaced by 1 cm, and 11 points along the vertical axis, also separated by 1 cm. See Fig.16. for reference. I used a Python script to read the table file and compute $B_y var$ at all points on the grid.

Fig. 16. Magnet gap transverse grid. The two dimensional transverse grid in the left magnet gap with respect to the LCS. The grid covers the top half of the dipole gap.

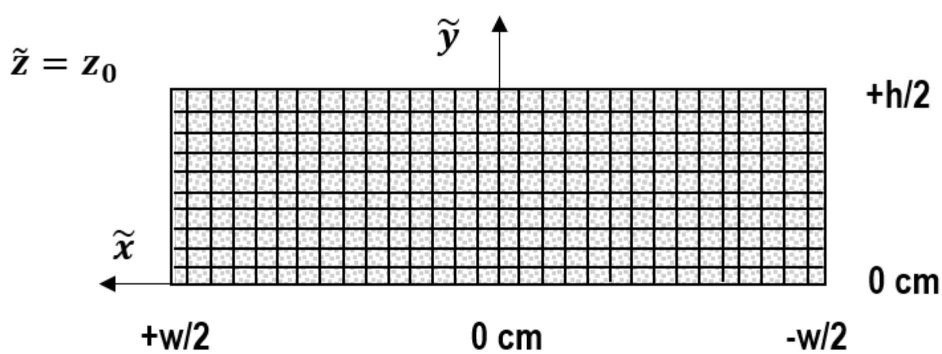

Since there is zero field contribution from B_x and B_z at the centre line, the variation of these component fields in the magnet gap cannot be computed in the same manner as was done for B_y. However, in order to get a sense of the outward change in $B_{x/z}$ in proportion to the central dipole field, $B_{x/z}(\tilde{x}, \tilde{y}, z_0)/B_0(z_0)$ were evaluated at every point on the same two dimensional grid.

2) Non-Linear Field Response: The effect of magnetic saturation in the septum magnet is a non-linear response of the field strength to an increase in coil current. Due to the spatial dependence of the $\vec{H}$ field, iron magnetization - and therefore saturation - occurs non-uniformly throughout the return yoke and pipe shield. For instance, the proximity of the shims to the high-field suggests that saturation should occur in this part of the yoke before it begins on the outer surface. This is similarly true in regions where the field lines are "pinched", such as at sharp corners or edges of the magnet. The relationship between the septum field strength and the power supply current was examined using the Tosca FEA simulations and the limited field measurements taken during the g2p experiment in Hall A. Table III contains the field measurements from probes that were positioned at four different locations inside the gap. These data were used to bound the Tosca FEA results.

TABLE III

MEASURED SEPTUM MAGNET FIELD DATA SETS

I_{ps} $[A]$	B_{S1} $[G]$	B_{S2} $[G]$	B_{S3} $[G]$	B_{BB} $[G]$
100	1397	1433	1447	1547
300	4195	4294	4342	4627
500	6978	7145	7245	7703
700	9621	9918	10074	10677
800	10758	11191	11389	12012
900	11736	12351	12610	13199
950	12153	12871	13165	13710

The septum field of the symmetric model was simulated by Tosca FEA for 15 current density settings from $J = -1500\ A/cm^2$ to $J = -100\ A/cm^2$, in increments of 100 A/cm^2. In the post-processor, a table of field values was generated for positions at the centre of the magnet gap and for combinations of vertical and horizontal offsets from the centre. This was done at three z-positions along the magnet length: at the edge, 5 cm inside the edge, and at the centre. The vertical offset is $+h/4$ and the horizontal offsets are $\pm w/6$ and $\pm w/3$. At each position in the magnet gap, an aggregate data set was created with 15 (I_i, B_i) simulated data pairs.

The field measurements were acquired when the septum magnet was configured with 3-coils. To compare the simulated field to the measured field the 3-coil equivalent power supply current was computed for each simulation. In the model a conductor pole has a total cross-sectional area of $A_{cs} = 80.64$ cm^2. The number of turns of a septum magnet pole is $N_t = 112$ in the 3-coil configuration and $N_t = 64$ in the 2-coil set-up. By (12) I_{ps} is calculated from J, A_{cs}, and $1/N_t$,

$$I_{ps} = JA_{cs}/N_t. \tag{34}$$

Table IV lists the corresponding I_{ps}, for both configurations, of the Tosca simulations.

Table IV

Equivalent Current Settings of Septum Magnet

Simulation	Single Pole	2-Coil	3-Coil
$\lvert J\rvert$ $[A/cm^2]$	Amp-Turns	I_{ps} $[A]$	I_{ps} $[A]$
100	8064	126	72
200	16128	252	144
300	24192	378	216
400	32256	504	288
500	40320	630	360
600	48384	756	432
700	56448	882	504
800	64512	1008	576
900	72576	1134	648
1000	80640	1260	720
1100	88704	1386	792
1200	96768	1512	864
1300	104832	1638	936
1400	112896	1764	1008
1500	120960	1890	1080

The relationship of the field strength to the current was, as an initial approximation, modelled by a linear equation of the form

$$B(I) = a_1 I + a_2, \tag{35}$$

where $B(I)$ is the predicted field strength and a_1 and a_2 are the fit parameters. Each data set was fit to this equation using the method of least-squares to determine the optimal parameter values. The field deviation from the corresponding predicted field strength was measured by the residual, defined at each point as,

$$\Delta B_i = B_i - B(I_i). \tag{36}$$

Since the uncertainty of each B_i measurement, σ_i, is unknown, the goodness of fit, χ^2, could not be determined for the regression line. Instead, an uncertainty common to all B_i measurements, σ, was estimated from the fitted data

$$\sigma \simeq \sqrt{\frac{\sum (\Delta B_i)^2}{n-2}}, \tag{37}$$

where n denotes the number of points used in the fit. The uncertainty of the fit parameters was estimated using equations [14]

$$\sigma_{a_1}^2 = \frac{n\sigma^2}{n\sum I_i^2 - \left(\sum I_i\right)^2} \tag{38}$$

and

$$\sigma_{a_2}^2 = \frac{\sigma^2}{n\sum I_i^2 - \left(\sum I_i\right)^2} \sum I_i^2. \tag{39}$$

In the next chapter I will show that a linear model of the field response to current, although decent as an initial approximation, is not appropriate for the entire data set. It can, however, be used to model a subset of the data where $I_{ps} \leq 500$ A. The regression line computed from the fitted data in the low-current region was used to predict the "zero saturation" field strength at high current ($I_{ps} > 500$ A). The percent residuals,

$$\frac{\Delta B_i}{B(I_i)}, \tag{40}$$

were examined in order to search for a systematic decline of the field strength.

3) Beam Line Field Integration in the Magnet Gap: The septum magnet is positioned upstream of the spectrometer arms to achieve the low scattering angle required for the CREX and PREX-2 experiments. The septum field integral specified for CREX is 1.21 Tm. This requires an aggressively high coil current, which had not been previously tested. In order to confirm the current setting that meets the CREX specification the central field integral was evaluated on the centre line of the left magnet gap, from $z = -100$ cm to $z = 100$ cm, for each Tosca simulation. This computation is done by the post-processor software. An aggregate data set was compiled of 15 (I_i, $\int B_i dz|_0$) data pairs. The central field integral was plotted against the current in order to observe the trend, which is below linear in the high current region.

The beam envelope is transported through the magnet gap inside a vacuum chamber at a small angle from the z-axis. Fig.17. shows the acceptance zone in the Hall A pivot region. I used the area cross-section of this vessel at the septum entrance and exit in order to estimate the acceptance region. At the entrance of the septum, the acceptance region is approximately -14 cm$\leq \tilde{x} \leq$-4 cm and -8 cm$\leq \tilde{y} \leq$8 cm. It expands vertically to the full gap height at the septum exit, -10 cm$\leq \tilde{y} \leq$10 cm, and horizontally to one half of the gap width, -6.8cm$\leq \tilde{x} \leq$8.2 cm. Because the electrons will passes through the magnet at positions -14 cm$\leq \tilde{x} \leq$8.2 cm and -10 cm$\leq \tilde{y} \leq$10 cm, due to vertical dispersion caused by the field, the change in the field integral in the total acceptance region was examined at the CREX current setting.

Fig. 17. Hall A pivot region. A top view of the Hall A pivot region as configured for CREX and PREX-2. This region contains the target vacuum chamber and the septum magnet. Also shown are the concrete shields, vacuum vessels and the central beam pipe.

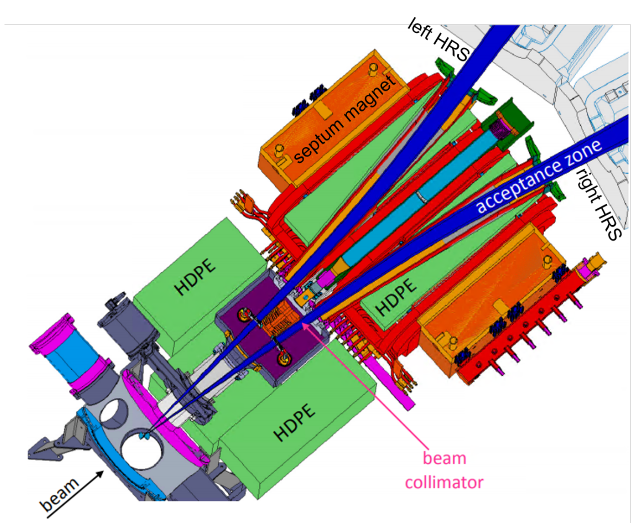

On the centre line the field is vertical and as such $\int B_y dz|_0 = \int B dz|_0$. Since B_x and B_z are in general non-zero off the longitudinal axis, the change in the vertical field integral, instead of the total field integral, is measured as a function of position on the transverse cross-section inside the gap. Using the post-processor, a two dimensional grid of $\int B_y dz$ values is generated and output as a table file. The grid contains 31 points along the horizontal axis and 21 points in the vertical, where each point refers to a position on the transverse slice. At each position the change in the field integral is computed from the equation

$$\frac{\Delta \int B_y(\tilde{x}, \tilde{y}, \tilde{z}) d\tilde{z}}{\int B_y(0, 0, \tilde{z}) d\tilde{z}} = \frac{\int B_y(\tilde{x}, \tilde{y}, \tilde{z}) d\tilde{z} - \int B_y(0, 0, \tilde{z}) d\tilde{z}}{\int B_y(0, 0, \tilde{z}) d\tilde{z}}. \tag{41}$$

The horizontal and axial field integrals are scaled by the inverse of $\int B dz|_0$ to measure the outward change in proportion to the central field integral.

4) Fringe Field in the Beam Pipe: The polarized electron beam is transported straight through the septum magnet toward the beam dump. An iron shield is used at the centre of the magnet to reduce the stray dipole field lines in the beam pipe and minimize the vertical and horizontal dispersion of the high energy beam. The total field integral at the centre of the beam pipe, evaluated in the direction of the beam line, from z=-100 cm to z=100 cm, is 0 Tm. However, off the longitudinal axis the field strength increases, in particular in the fringing region, and will cause some deflection of the charged particles. This effect is measured with the field integral through the pipe.

I use a cylindrical coordinate system for field analysis at the centre of the septum magnet:

$$\rho = \sqrt{x^2 + y^2}, \quad \theta = \arctan\left(\frac{y}{x}\right), \quad z_p = z. \tag{42}$$

The transverse cross-section in the beam pipe gap is a circle defined with radius $r = 3.5$ cm, shown in Fig.18..

Fig. 18. Beam pipe transverse cross-section. A transverse cross-section of the centre beam pipe gap with respect to the LCS.

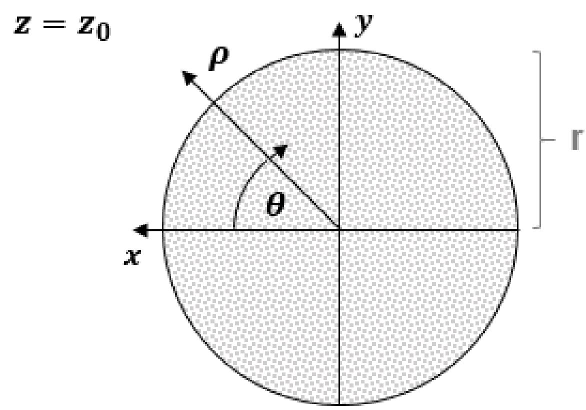

The change in $\int Bdz$ is computed for the first quadrant of the cross-section. Since there are reflections of the field in the xz and yz global coordinate planes, analysis of one quadrant is sufficient. In the post-processor, a two dimensional grid of $\int Bdz$ is generated and output as a file. The grid is composed of 10 radial lines from the centre to the perimeter of the cross-section, each separated by 10°, and 7 arcs, each separated radially outward by 0.5 cm. See Fig.19. for reference.

Fig. 19. Shield gap transverse grid. The two dimensional transverse grid in the beam pipe with respect to the LCS. This grid covers one quadrant of the shield gap.

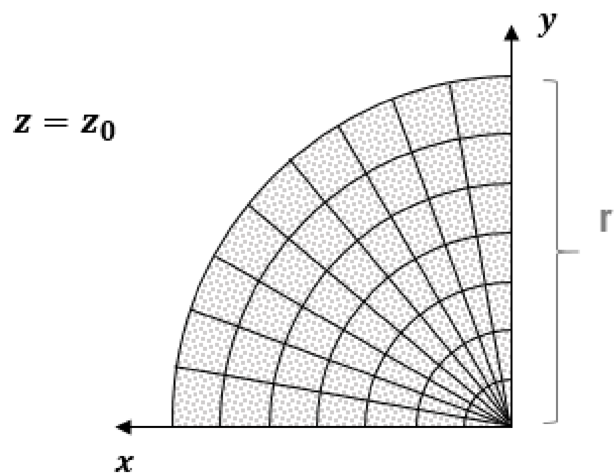

IV. Results

I've organized this chapter into two sections. In the first section, I present the results of the field response curve in the magnet gap. The magnetic flux density in the septum high-field regions is induced by the current-supplied coils and the magnetized iron materials. Though the permeability of the material is assumed to be isotropic and homogeneous, magnetization throughout is non-uniform due to the spatial dependence of the $\vec{H}$ field. As magnetized segments of the return yoke and pipe shield begin to saturate in response to a strong local H field their contributions to the magnetic flux density become non-linear. Therefore the relationship between B and the current that is supplied to the coils, I_{ps}, is not straightforwardly linear or uniform. Field measurements of the septum magnet acquired by the g2p collaboration were analyzed and used as a point of comparison for the Tosca simulations. These results are presented first, followed by the field response of the Tosca simulations. Since the magnetization of the iron yoke is non-uniform, the field turnover was examined at a few vertical and horizontal offsets from the magnet gap centre. These results are shown and compared to the measured field data.

The septum magnet bend angle specified for CREX requires a greater operating current than used for PREX-2, one that needs to be confirmed by field simulations. Since magnetic saturation of the iron materials is expected at high current, the degree to which this limits the septum field strength and affects the field homogeneity inside the magnet gap determines the suitability of this septum magnet for CREX. The CREX current setting can be found by examining the central dipole field integral dependence on coil current. I begin the second section of this chapter with this result and follow it with a look at the field integral variation inside the acceptance region of the magnet gap at the CREX current setting. These provide upper and lower bounds to the central field integral, and therefore the central bend angle, within the acceptance region of the magnet. Another concern is the significant impact that magnetic saturation has on the capability of the centre shield to minimize the fringing field at the beam pipe and drop the field strength inside the magnet, which is imperative in the safe transport of the high-energy beam. In the second part of this section I present evidence of strong saturation in the original septum shield at current settings above 500 A and show it's effects on the field throughout the beam pipe. To mitigate the non-linear effects inside the beam pipe, the shield may be modified with upstream and downstream extensions of the same material. I end this chapter by presenting the results of field analysis of the modified septum model.

A. Non-Linear Field Response inside the Magnet Gap

1) Hall A Field Measurements: The field strength of the septum magnet was measured in Hall A during the g2p experiment. There are four sets of field data taken at different positions inside of the magnet gap. These are referred to as S2, BB, S1, and S3 in the figures. Using a single-axis probe, the vertical magnetic flux density was measured at each location for seven current settings. In this region of the septum, B_y is positively and, as a first approximation, linearly dependent on the current supplied to the coils, as shown in Fig.20.. The vertical error bars in the figure are σ_{all}, estimated from the linear fit of all points ($n = 7$) in each data set (see (37) for reference). These and the fit parameters are listed in Table V. There is a slight curvature in the data that is more clearly evident from the residuals, which trend parabolic (Fig.21.).

Fig. 20. Field measurements taken in the Hall A septum magnet during g2p.

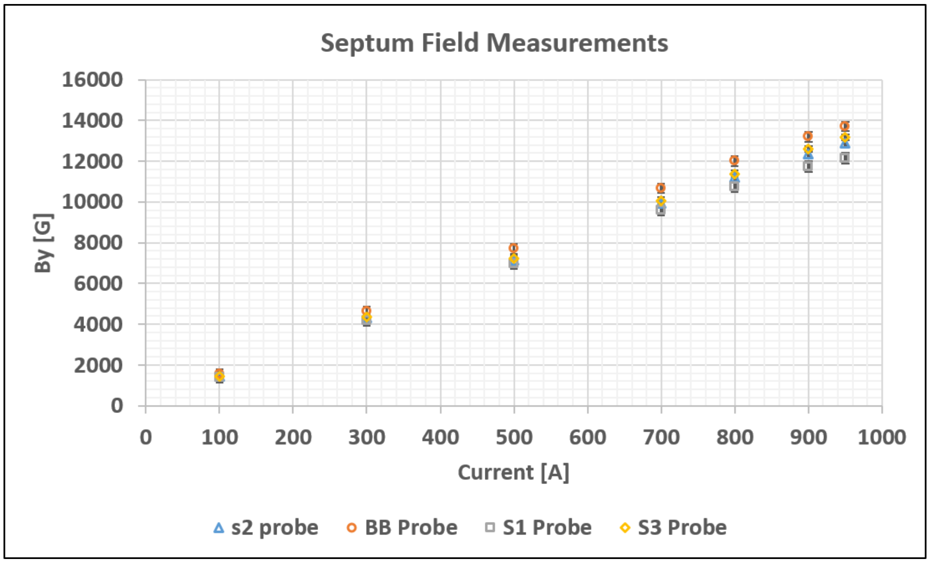

Table V

Fit Parameters of Measured Field Data Sets (n=7)

Linear Fit ($n = 7$)	s2	bb	s1	s3
$a_1 \pm \sigma_{a_1}$	13.6±0.2	14.4±0.3	12.8±0.4	13.9±0.2
$a_2 \pm \sigma_{a_2}$	227±153	297±202	356±237	185±132
σ_{all}	178	234	274	153

Fig. 21. Residuals of the Hall A septum field data.($n = 7$ points fitted)

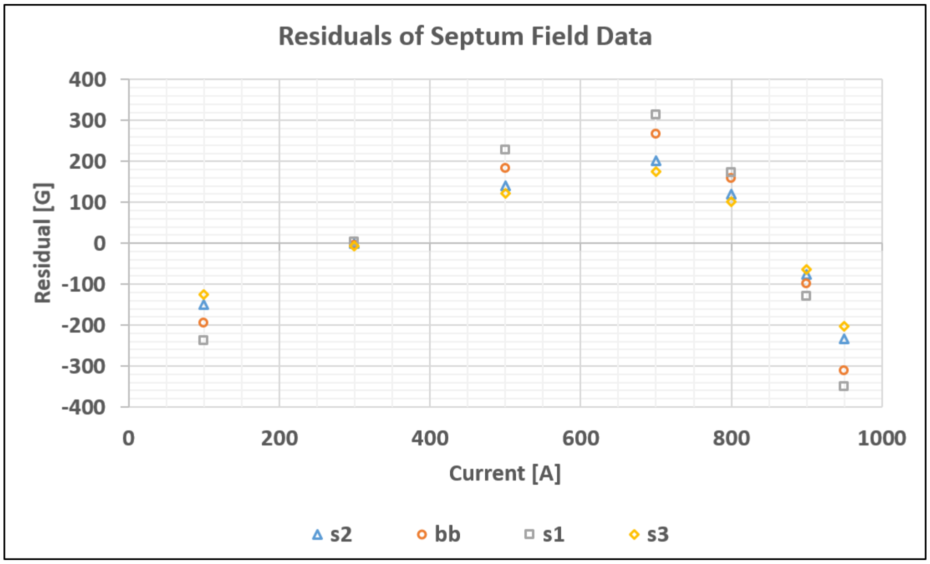

A linear regression model is better suited for a subset of each set of field measurements, one which omits points in the high current regime where the relationship between B_y and the current is non-linear due to growing saturated segments of iron materials. The low current data subsets include 3 data points for which $I_i \leq 500A$. These data were fit to a least-squares regression line (Fig.22.). The residuals (Fig.23.) from this fit are significantly smaller than those of the $n = 7$ fit, the standard deviation, σ_{low}, being less than 3% of σ_{all} (Table VI).

Fig. 22. Linear fit of the low current subset ($I_i \leq 500$ A) of the septum field data. ($n = 3$ points fitted)

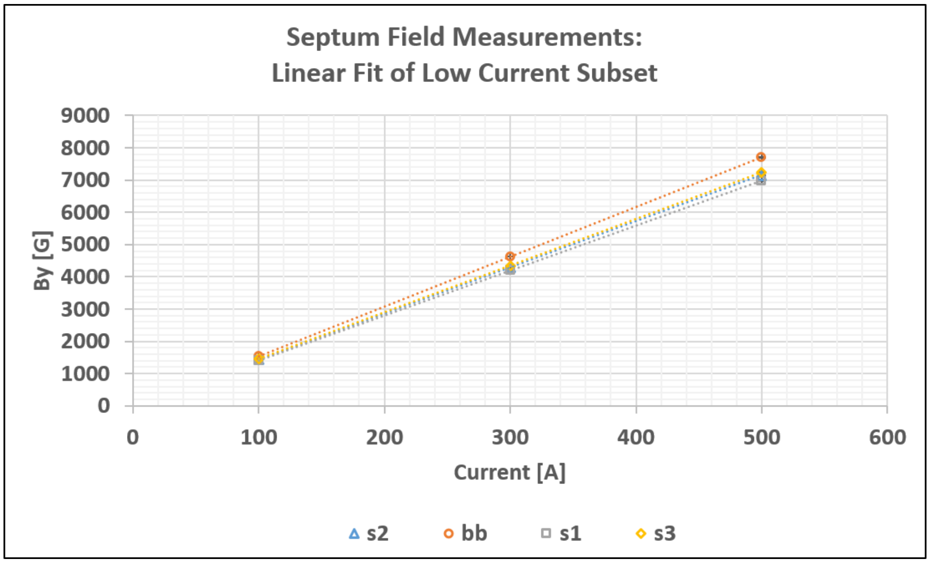

Table VI

Fit Parameters of Low-Current Data Subsets (N=3)

Linear Fit ($n = 3$)	s2	bb	s1	s3
$a_1 \pm \sigma_{a_1}$	14.28±0.01	15.390±0.006	13.95±0.02	14.50±0.01
$a_2 \pm \sigma_{a_2}$	7±5	9±2	4±7	-4±4
σ_{B_y}	4	2	6	3

Fig. 23. Linear residuals of the septum field data for $I_{ps} \leq 500\ A$. ($n = 3$ points fitted)

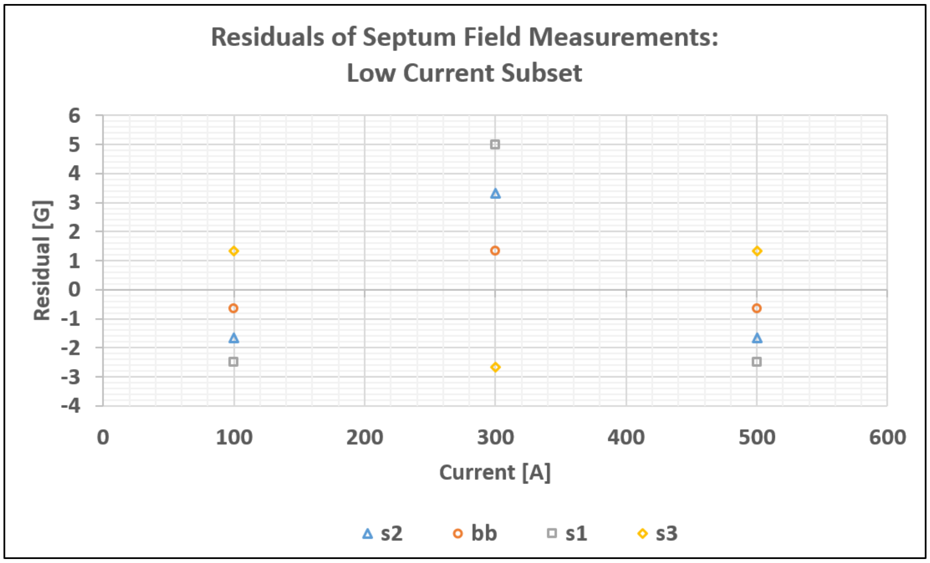

To measure the systematic decline of the field strength for current settings above 500 A, the low current regression line is extrapolated to 950 A. Fig.24. contains the field data plotted against the "zero saturation" prediction field strength. It shows the data above 10 kG slowly curving downward from the $B_{y,measured} = B_{y,prediction}$ line (black, dashed line). The field deviations from linear are shown in Fig.25.. They steadily decline, at different rates across all four data sets, to between -4.3% and -8.3% at 950 A.

Fig. 24. Measured field strength vs the predicted *zero saturation* field strength of the Hall A field measurements over the entire sampled current range. The black dashed line is $B_{y,measured} = B_{y,predicted}$.

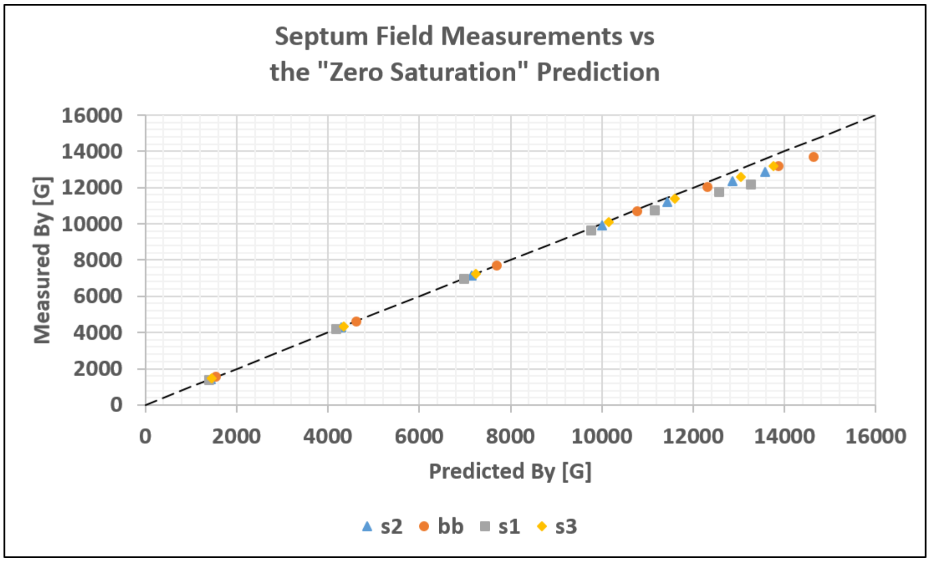

Fig. 25. Field deviation of the Hall A septum data from the *zero saturation* prediction.

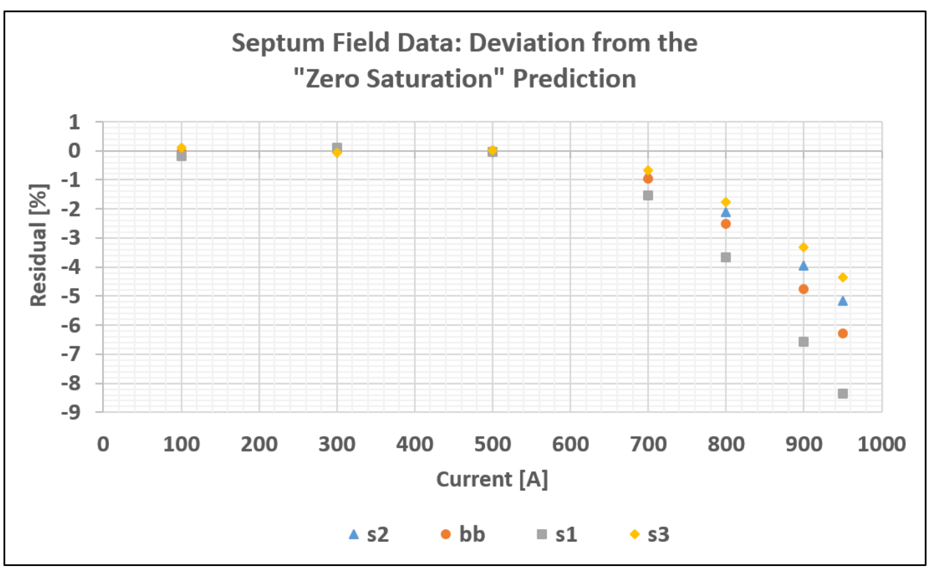

2) Tosca Simulations: The central dipole field $\vec{B}_0(z)$ refers to the septum field on the centre line of the magnet gap. I make this distinction because the variation of the field inside the magnet is measured with respect to the field at the dipole centre. The longitudinal dependence of $B_0(z)$ is most evident in the fringing region of the magnet. The Tosca simulations reproduce a practical fringe field in which the gradient $dB_0(z)/dz$ in the direction of the beam line is non-constant in the fringing region. See Fig.26. for reference. Due to this so-called edge effect the full central field magnitude is achieved at some distance *inside* the upstream edge, at which point the field is fairly constant until some distance inside the downstream edge.

Fig. 26. The gradient of the central dipole field, $\frac{d}{dz}B_0(z)$, in the direction of the beam line; shown for a few current density settings.

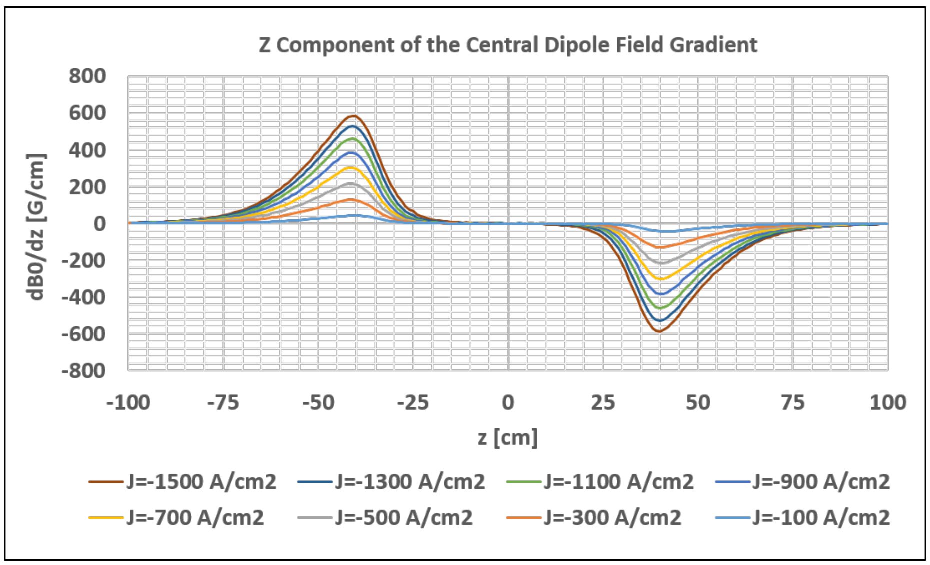

The beam envelope passes through the magnet gap inside the vacuum vessel which is positioned through the dipole at a angle to the z axis. I used the area cross-section of the vacuum vessel to estimate the acceptance region at the septum entrance and exit. At the entrance of the septum, the acceptance region is approximately -14 cm $\leq \tilde{x} \leq$ -4 cm and -8 cm $\leq \tilde{y} \leq$ 8 cm. It expands vertically to the full gap height at the septum exit, -10 cm $\leq \tilde{y} \leq$ 10 cm, and horizontally to one half of the gap width, -6.8

cm $\leq \tilde{x} \leq$ 8.2 cm. I examined the variation of the vertical field component within the magnet gap at the edge, 5 cm inside the edge, and at the centre. $B_y var$ is plot against the vertical position in the dipole at 12 horizontal positions that cover the width of the total acceptance region. Results are shown for the fields simulated at J= -500 A/cm^2, -1000 A/cm^2, and -1500 A/cm^2 (Fig.27., 28., 29.). Through the length of the magnet gap, the variation of B_y from the central field skews positive and is greatest at the top of the gap. $B_y var$ has both horizontal and vertical dependence. However, there is a region at the centre of the magnet, -5 cm$\leq \tilde{x} \leq$+5 cm, where it is fairly constant, between -1% and $+2\%$ of the central field. Magnetic saturation appears to have the greatest effect at the magnet edge near the top of the gap ($\tilde{y} > 6$ cm, roughly), causing a significant drop in the variation of the field, from around +75% at J= -500 A/cm^2 down to around +40% at J=-1500 A/cm^2.

Fig. 27. The variation of B_y within the bounds of the magnet gap, simulated for J= -500 A/cm^2 coils.

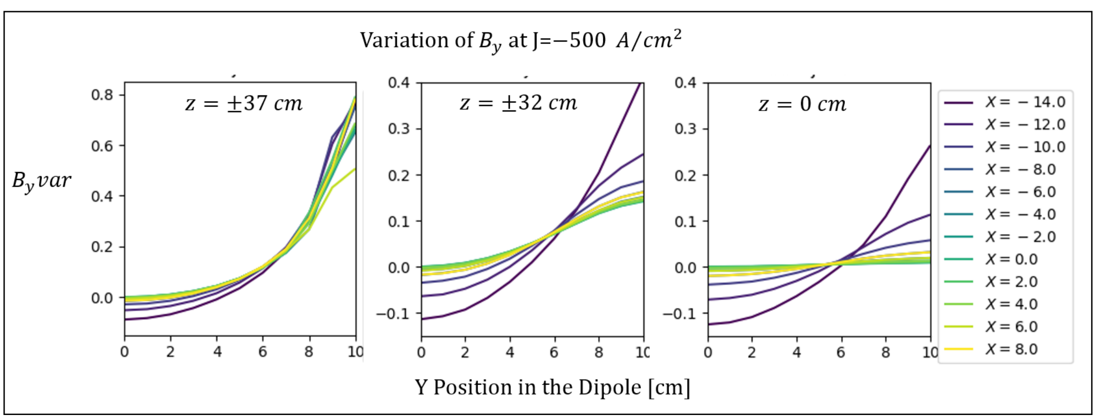

Fig. 28. The variation of B_y within the bounds of the magnet gap, simulated for J= -1000 A/cm^2 coils.

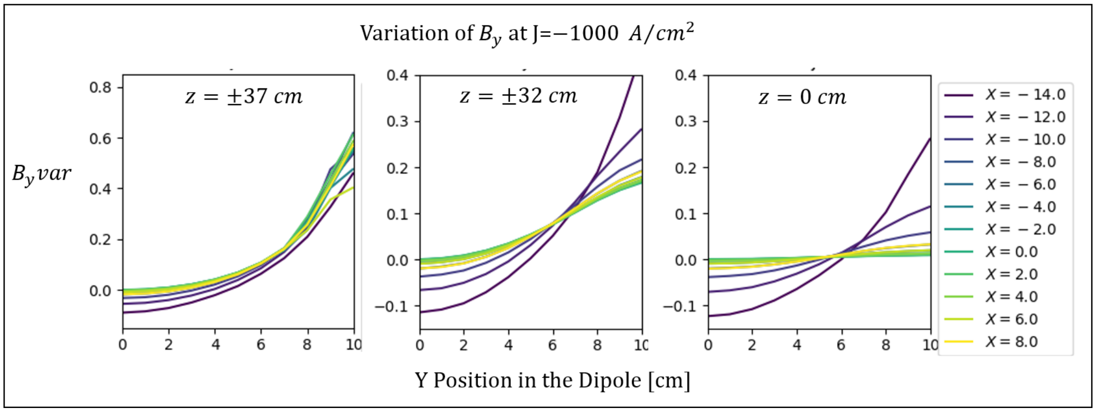

Fig. 29. The variation of B_y within the bounds of the magnet gap, simulated for J= -1500 A/cm^2 coils.

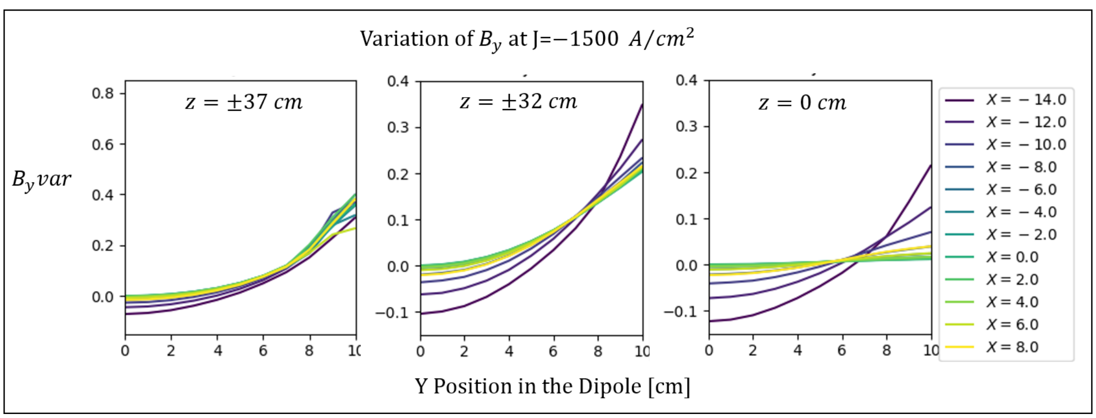

The maximum central dipole field, evaluated at $\tilde{x} = 0$ cm, $\tilde{y} = 0$ cm, and $\tilde{z} = 0$ cm (left magnet gap), is bounded by the Hall A septum field measurements (Fig.30.). Measurement uncertainty was likewise estimated from the linear fit of the Tosca data, which are $n = 15$ points. The linear residuals are smaller in scale than those of the field measurements, however, they are similarly parabolic (Fig.31.). I used the same low current region, $I_{ps} \leq 500$ A, to fit the linear part of the curve, which are $n = 6$

data points. The field turnover is slower than the empirical data, declining to less than 1% at 1080 A (Fig.32.).

Fig. 30. The current dependence of the central dipole field. The Tosca field strength was evaluated at $\tilde{x} = 0$ cm, $\tilde{y} = 0$ cm, and $\tilde{z} = 0$ (Left magnet gap). Superimposed are the Hall A septum field data.

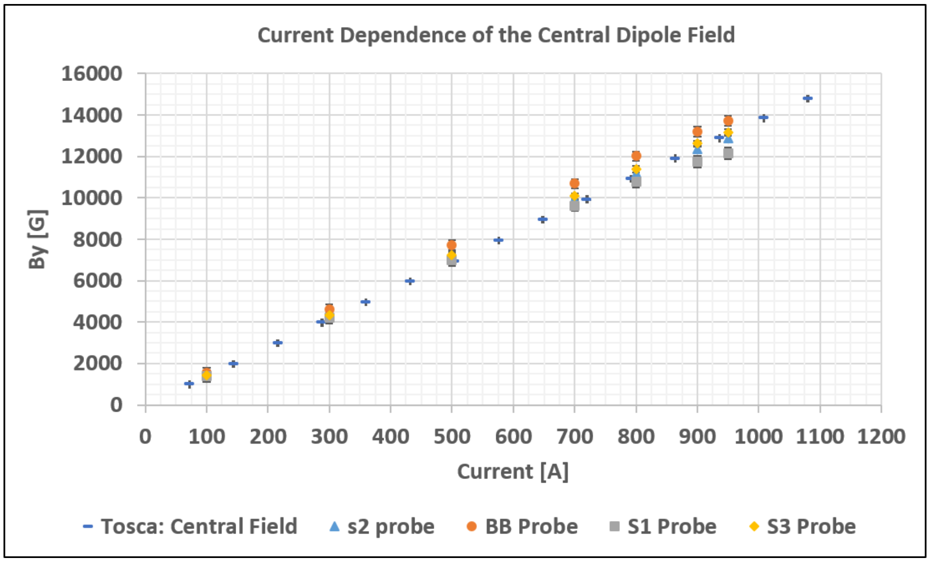

Fig. 31. Linear residuals of the maximum central dipole field calculated by Tosca. ($n = 15$ points fitted)

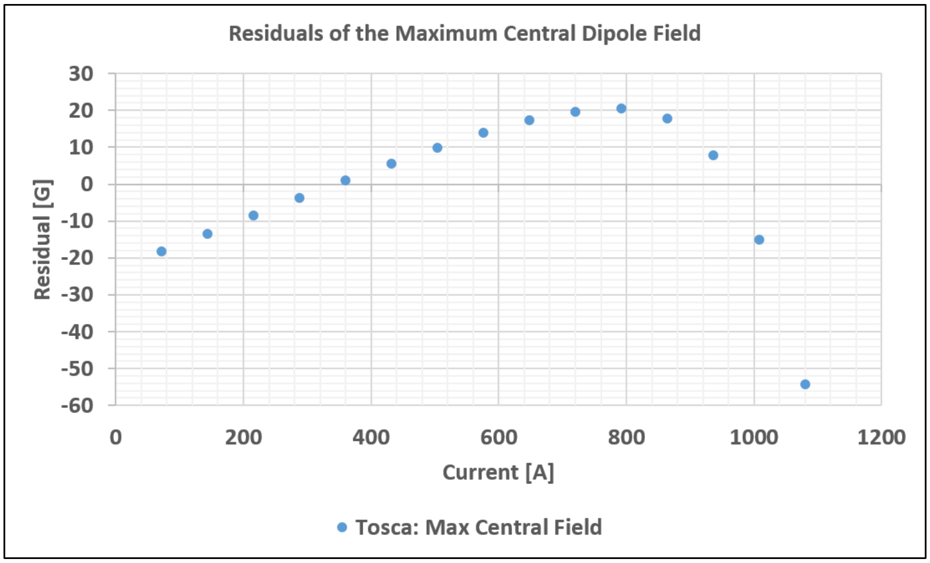

Fig. 32. Field deviation of the maximum central field from the *zero saturation* prediction equation. The Hall A septum field data are indicated with black lines.

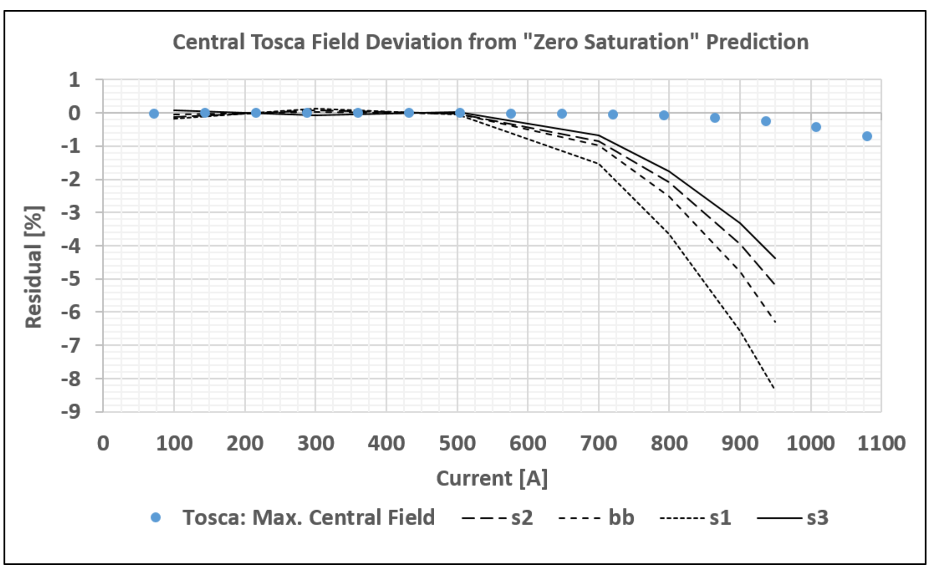

The Tosca dipole field was evaluated at a few vertical and horizontal offsets from centre to confirm field agreement with the measurements. On the $\tilde{y} = 0$ cm plane, the field strength at current settings above 500 A (high current region) is spread vertically and below the maximum central field, which corresponds to horizontal and longitudinal position offsets (Fig.33.). At $\tilde{x} = \pm w/3$ and $\tilde{z} = -32$ cm (5 cm inside the upstream edge of the magnet), the Tosca field data lies under the lower bound that is suggested by the s2 probe field measurements. The vertical spread in the field strength is less drastic on the $\tilde{y} = +h/4$ cm plane, but evident, in particular, at $\tilde{z} = -32$ cm (Fig.34.). These data are within the upper and lower bounds of the Hall A septum field measurements.

Fig. 33. The Tosca field evaluated at a few horizontal offsets on the $\tilde{y} = 0$ cm plane near the upstream edge and mid-length of the magnet gap. Superimposed on the Hall A septum field data. For clarity, the results are shown for the high current region only.

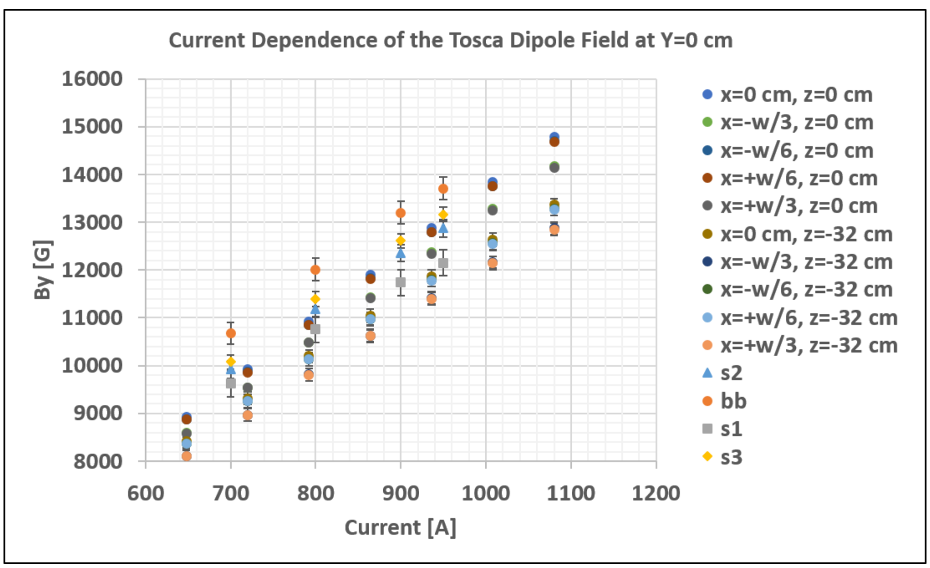

Fig. 34. The Tosca field evaluated at a few horizontal offsets on the $\tilde{y} = +h/2$ plane near the upstream edge and mid-length of the magnet gap. The Hall A septum data was superimposed for comparison. Results are shown for the high current region only.

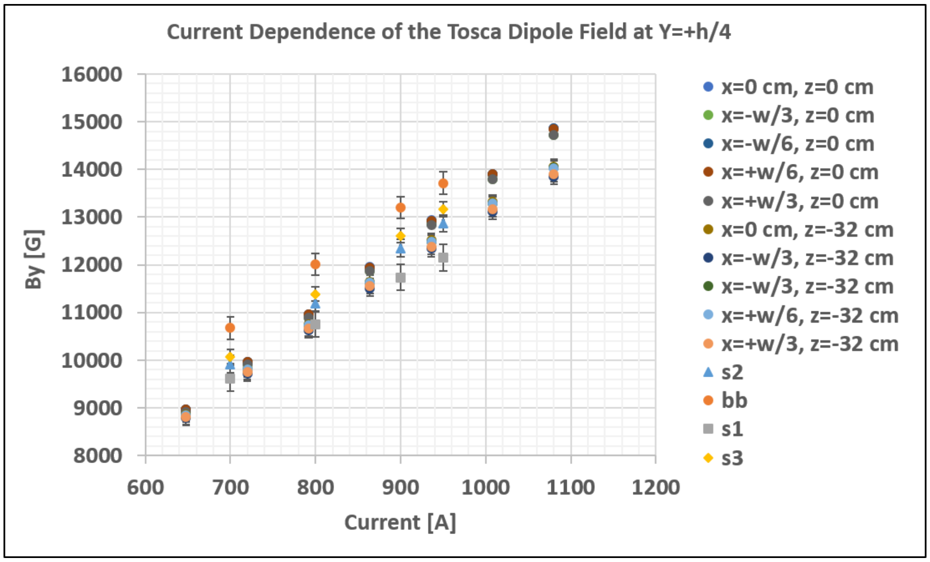

At the mid-length of the magnet gap the Tosca field turnover is minimal, dropping to between -0.6% and -1.2% at 1080 A (Fig.35.). The field curvature near the upstream edge of the magnet nearly reproduces the empirical results, particularly in the range 500 A$\leq I_{ps} \leq$800 A (Fig.36.). However, above 800 A the field turnover is not as fast in comparison. For example, at 936 A the Tosca residuals are between -2.5% and -3.4%.

Fig. 35. The field deviation from the *zero saturation* prediction line. Included are the Tosca fields evaluated at the mid-length of the magnet and a combination of x and y offsets from the centre.

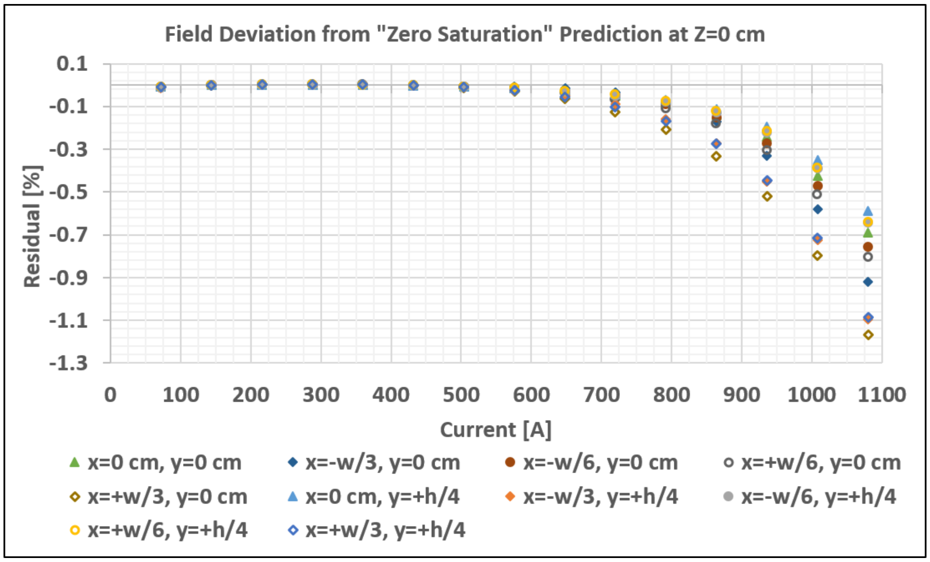

Fig. 36. The field deviation from the *zero saturation* prediction line. Included are the Tosca fields evaluated near the upstream edge of the magnet and a combination of x and y offsets from the centre. The Hall A septum field data are shown as black lines.

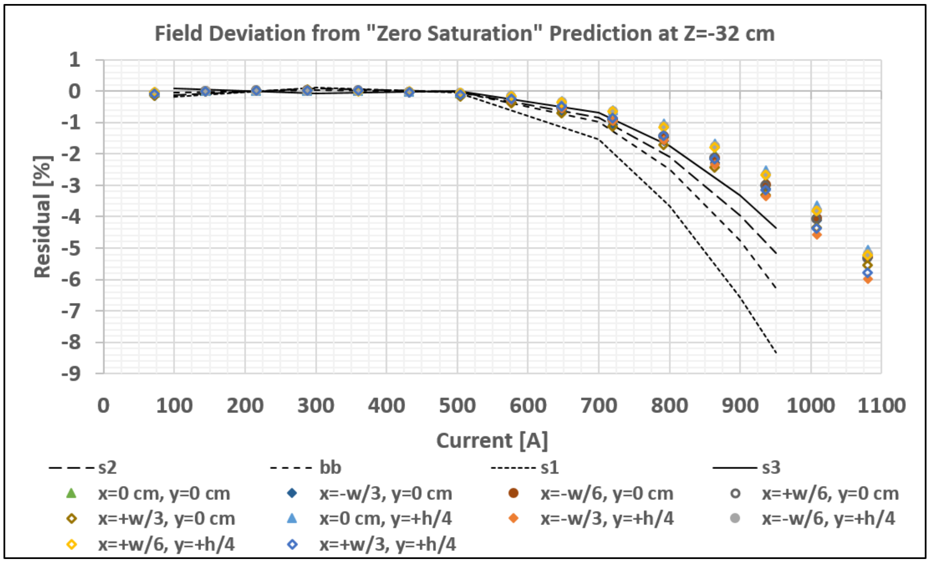

B. Septum Magnetic Field at the CREX Current

1) Central Field Integral in the Magnet Gap: The septum bend radius specified for CREX requires a central dipole field integral of $\int Bdl|_0 = 1.21$ Tm. The Tosca simulations indicate that within the operating current range of the power supply (max. 1050 A) the dipole field strength produced by the 2-coil septum magnet is too low. However, with an additional coil at every pole of the magnet, the specified field magnitude can be achieved. The central dipole field integral, evaluated on the centre line of the magnet gap from z=-100 cm to z=100 cm, is shown as a function of current in Fig.37.. Results were scaled to show the field magnification possible with a coil addition at each pole. At J=-1300 A/cm^2, the field integral computed from the Tosca simulation is $\int B_y dl|_0 = 1.193$ Tm. This pin points the CREX current at approximately 936 A in the 3-coil magnet configuration.

Fig. 37. The central field integral as a function of current, evaluated in the direction of the beam line. Results are shown for the septum magnet in the 3-coil and 2-coil configurations.

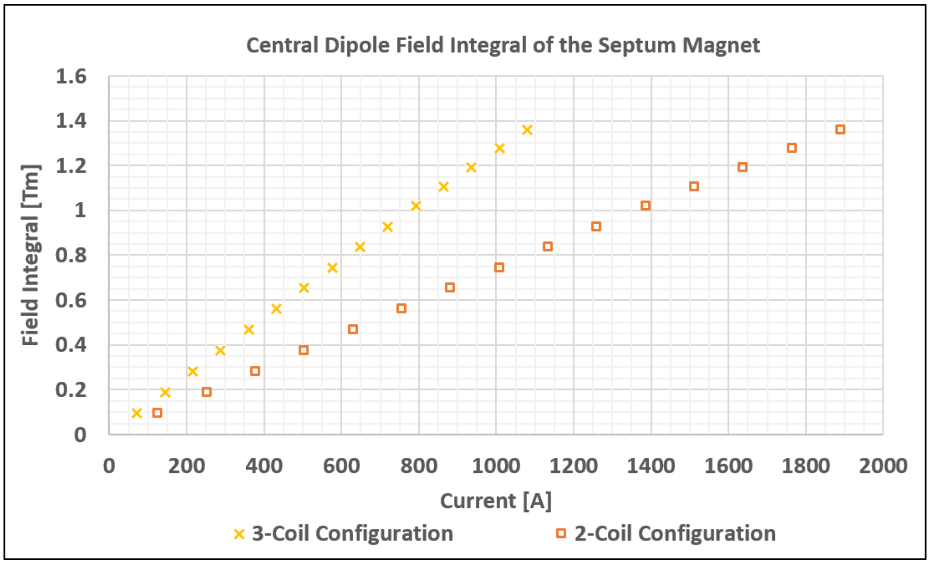

I examined the change in the central field integral within the acceptance region of the magnet gap in order to place an upper and lower bound on the CREX Bdl measurement. On the centre line the field is vertical and as such $\int B_y dz|_0 = \int Bdz|_0$. Off-centre, $\tilde{x} \neq 0$ cm or $\tilde{y} \neq 0$ cm, B_x and B_z are in general non-zero. Therefore, the changes in $\int B_x dz$ and $\int B_z dz$ were computed in addition to the vertical field integral. The results are scaled by the inverse of $\int Bdl|_0$. $\Delta \int B_z dz$ is 0 ± 0.004 Tm, negligible as compared to the central field integral, and is not shown. Fig.38. contains 3D wire plots which show the change in the field integral (vertical and horizontal components) as a function of position on the transverse plane inside the gap.

Fig. 38. A 3D wire plot of the change in the field integral as a function of position; evaluated inside the magnet gap. Simulation is $J = -1300$ A/cm^2.

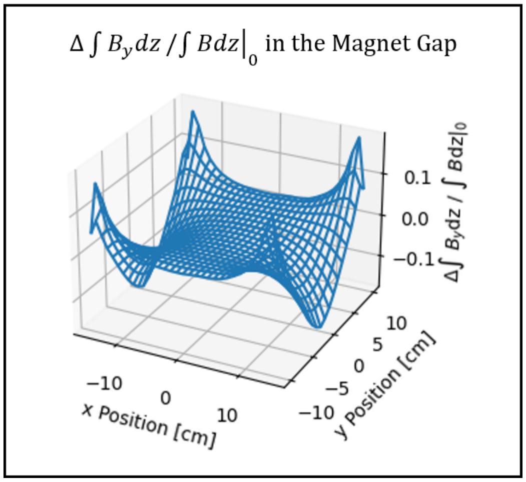

(a) Vertical component

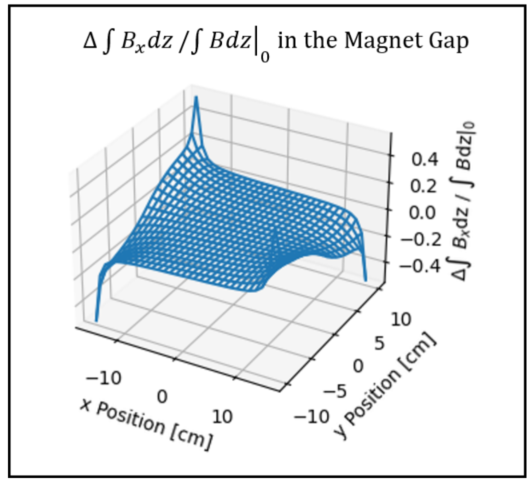

(b) Horizontal component

The variation in $\int B_y dz$ is greatest at the inner edge of the acceptance region, $\tilde{x} = -14$ cm (Fig.39.). At this fixed horizontal position, $\Delta \int B_y dz$ changes along the vertical axis in a parabolic fashion, from +17.4% at $\tilde{y} = -10$ cm, down to -13.0% at $\tilde{y} = 0$ cm, and rises up to +17.4% at $\tilde{y} = +10$ cm. For approximately four-fifths of the acceptance width, -10 cm$\leq \tilde{x} \leq$8 cm, the vertical field integral is within ±5% of the central value, or, ±0.06 Tm, at all vertical levels from the bottom to the top shim. Similarly, the variation in the horizontal field integral is greatest at $\tilde{x} = -14$ cm. Here, $\Delta \int B_x dz$ is sinusoidal in the direction of the vertical axis. The variation is ±17.7% at $\tilde{y} = \pm 10$ cm, and zero at the mid-plane (Fig.40.). In the region -10 cm$\leq \tilde{x} \leq$8 cm, the change in $\int B_x dl$ is between ±5.5% of $\int Bdz|_0$, which corresponds to ±0.066 Tm.

Fig. 39. The change in the line integral of B_y as a fraction of the central field integral; evaluated inside the total acceptance region.

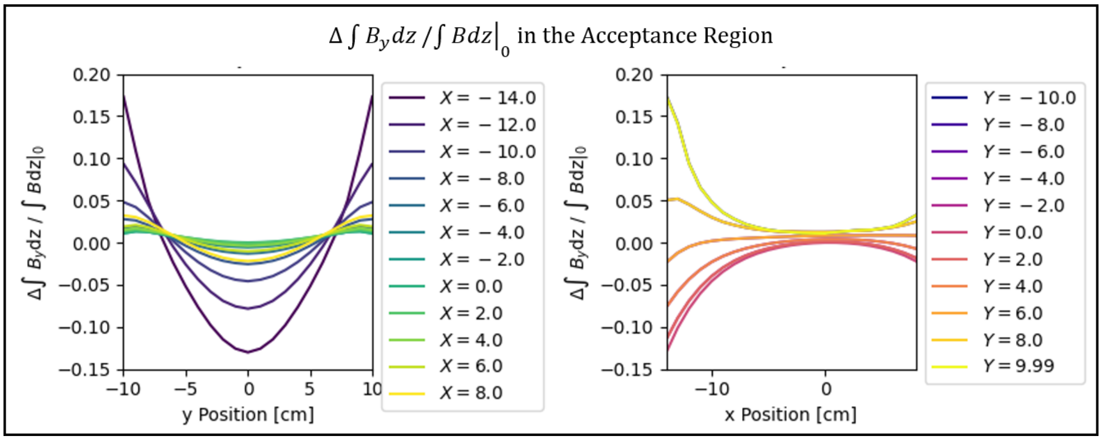

Fig. 40. The change in the line integral of B_x as a fraction of the central field integral; evaluated inside the total acceptance region.

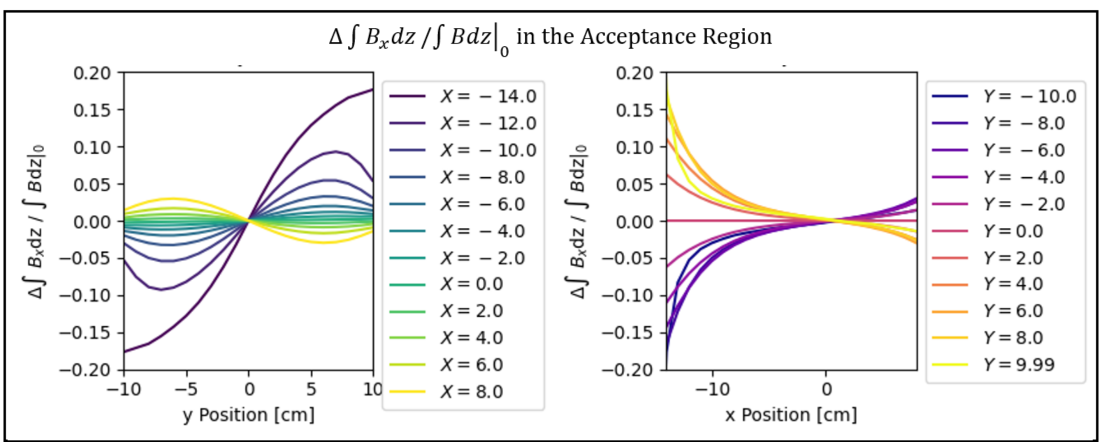

2) Fringe Field Reduction in the Beam Pipe: The polarized electron beam is transported straight through the septum magnet toward the beam dump. To ensure minimal deflection of the high energy beam an iron shield is used inside the magnet, which reduces the stray field lines within the beam pipe. Inside the shield the field strength is non-zero at positions radially outward from the centre. In fact, at the CREX current, it is up to $\sim 25\%$ larger than the maximum fringe field near the perimeter of the pipe (Fig.41.). This is not the case for the septum operated at a low current, where the field strength drops significantly once inside the magnet and therefore the fringe field at the upstream and downstream edges is the main contributor to the total field integral through the pipe. At every current setting that was examined, the total field integral is 0 Tm at the centre of the pipe and increases radially outward. This results in vertical and horizontal dispersion of the beam for particles off the longitudinal axis. The change to the $\int Bdl$ at high current is non-linear as field lines can no longer be adequately contained by the saturated shield (Fig.42.).

Fig. 41. Symmetric short shield: The total field strength as a function of z in the beam pipe at the CREX current.

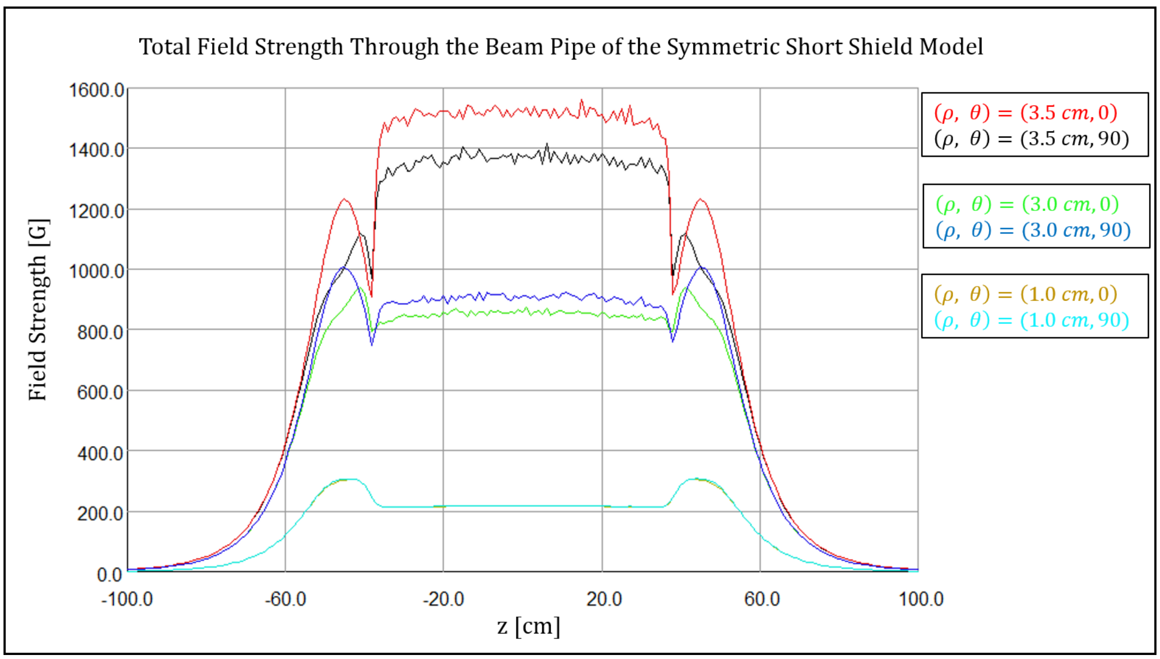

Fig. 42. Symmetric short shield: The change in the total field integral inside the pipe in response to current increase.

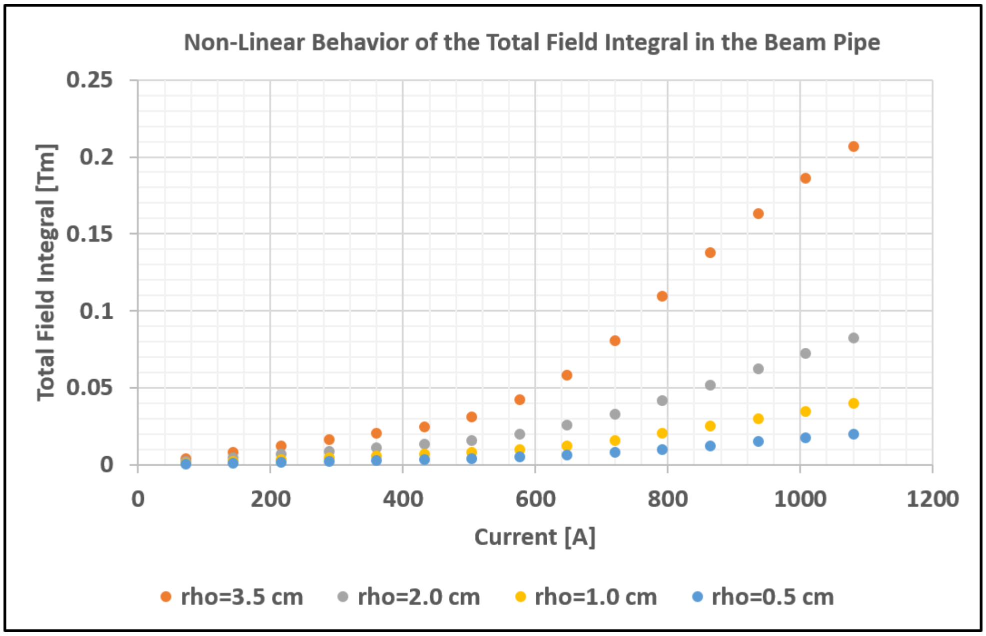

At the CREX current, the strong radial dependence of $\int Bdl$ becomes non-linear near the perimeter of the beam pipe (Fig.43.). This coincides with a growing θ dependence which is most prominent at $\rho = 3.5$ cm, where the total field integral is largest (Fig.44.). The maximum $\int Bdl$ at the perimeter is 0.163 Tm ($\theta = 0$ deg) and 0.149 Tm ($\theta = 90$ deg). As shown in Fig.43., the line integrals of B_x and B_y are complementary in that $\int B_x dl$ is maximum at $\theta = 0$ deg where $\int B_y dl$ is minimum and the inverse at $\theta = 90$ deg. The line integral of B_z through the beam pipe is negligible. Since the shield does not adequately minimize the field inside the pipe a shield extension at the upstream and downstream edges was proposed to mitigate the effect of the magnetic saturation.

Fig. 43. Symmetric short shield: The total field integral and component field integrals as a function of transverse position in the beam pipe.

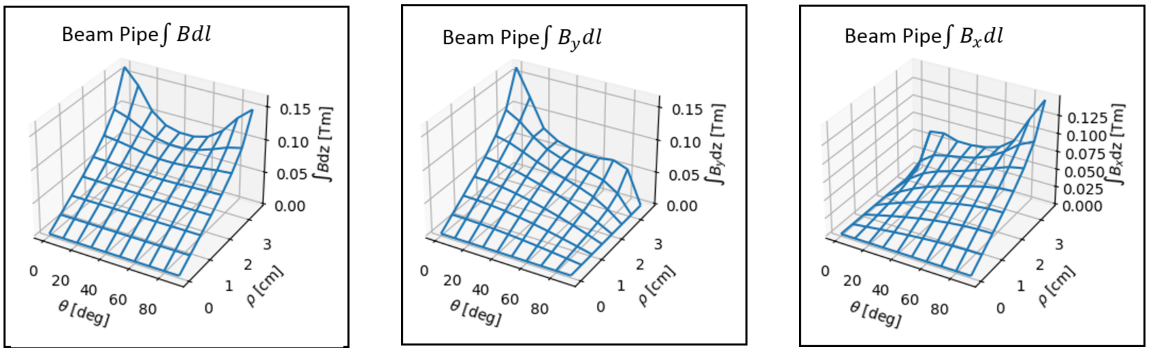

(a) Total Bdl (b) Vertical component (c) Horizontal component

Fig. 44. Symmetric short shield: The ρ and θ dependence of the total field integral in the beam pipe.

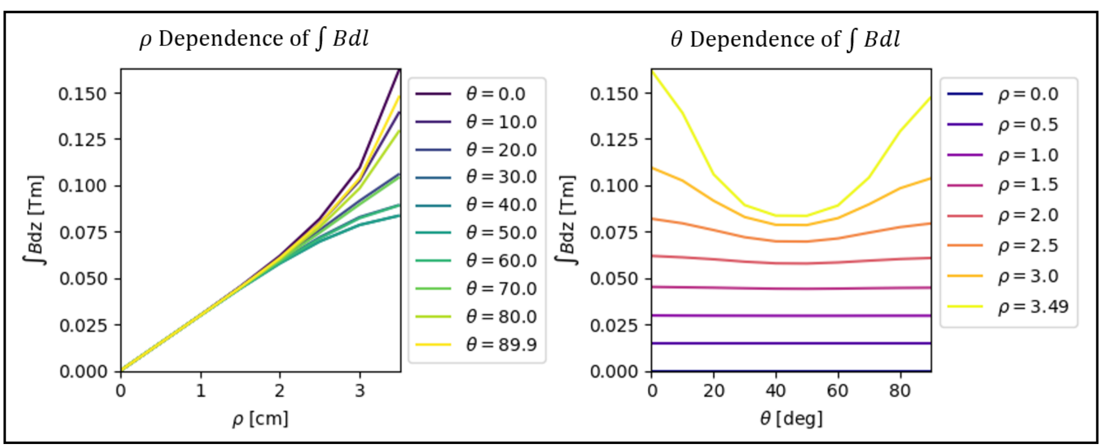

A new model of the septum magnet was created with a modified centre shield and solved with Tosca FEA. The shield can be extended to -69 cm at the upstream edge and only up to 61 cm at the downstream edge due to the proximity of the HRS quads. Fig.45. shows the field strength in the beam pipe as a function of z. The fringe field, observed off the longitudinal axis, is asymmetric at the new shield edges. Additionally, the field inside the shield is non-zero but non-uniform. The field strength initially drops inside the upstream edge then gradually increases along z where it reaches a maximum near the centre of the magnet and drops before the downstream edge. This is a clear indicator of some magnetic saturation in the shield, however B near the perimeter of the pipe is under 300 G, which is a factor > 4 smaller than what was observed with the original shield.

Fig. 45. Asymmetric extended shield: The total field strength as a function of z in the beam pipe.

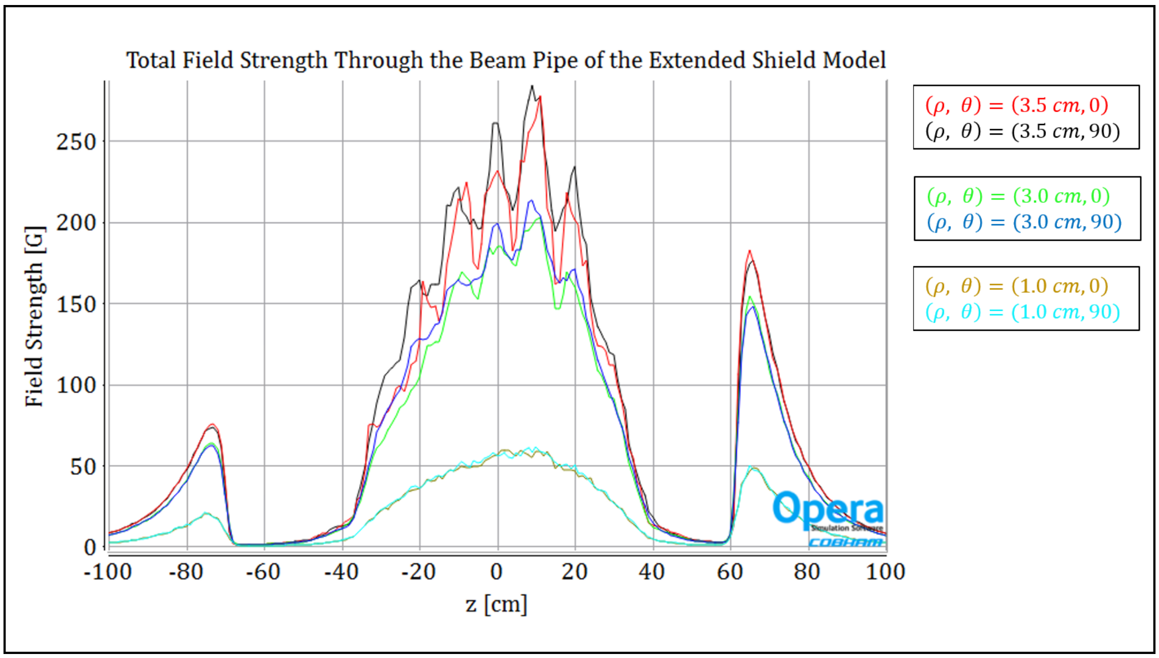

The significant reduction of field lines through the pipe is reflected in the total field integrals, shown in Fig.46., which are an order smaller than the results of the symmetric short shield model. The radial dependence of $\int Bdl$ is slightly non-linear around $\theta = 45$ deg which similarly coincides with the θ dependence evident near the perimeter (Fig.47.). At $\rho = 3.5$ cm the maximum $\int Bdl$ is 0.0164 Tm ($\theta = 90$ deg) and 0.0154 Tm ($\theta = 0$ deg). These are smaller than the maximum field integral

Fig. 46. Asymmetric extended shield: The total field integral and component field integrals as a function of transverse position in the beam pipe.

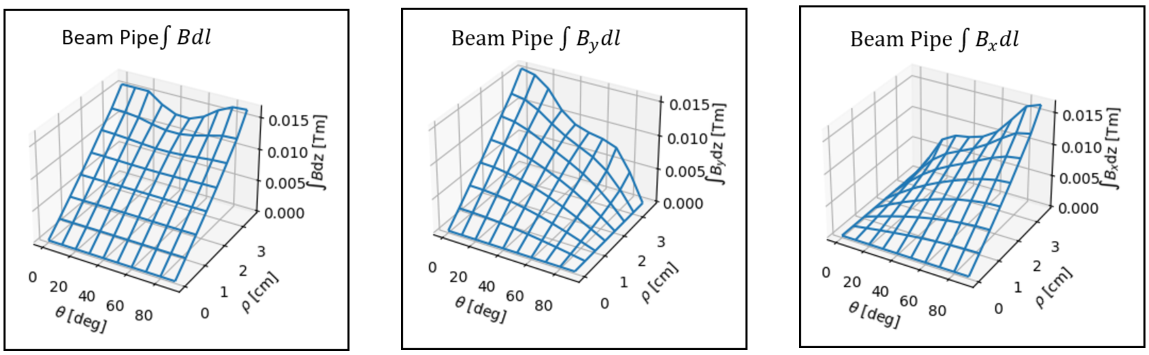

(a) Total Bdl (b) Vertical component (c) Horizontal component

that was computed for the original shield at the PREX current setting, which was acceptable for the septum magnet to be used during the PREX-1 experiment.

Fig. 47. Asymmetric extended shield: The ρ and θ dependence of the total field integral in the beam pipe.

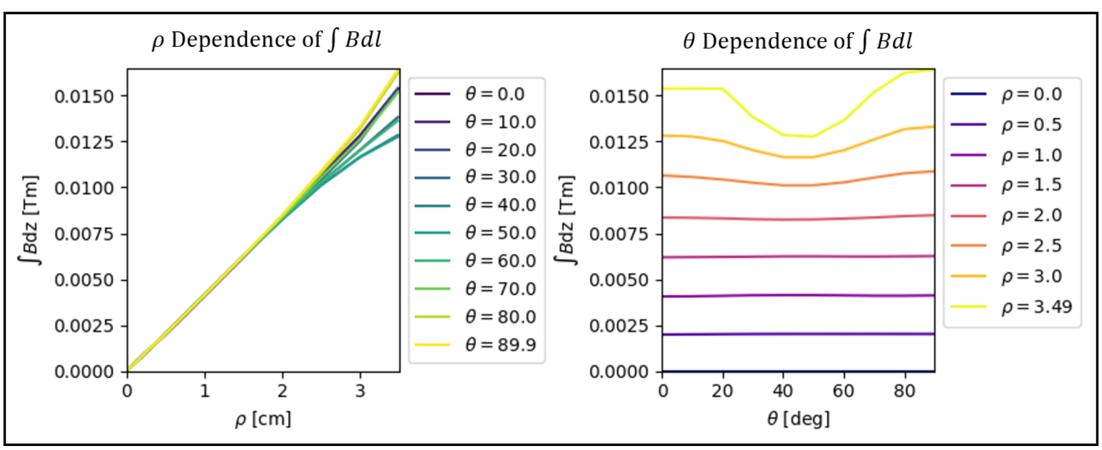

V. Summary and Conclusions

PREX-2 and CREX are very forward angle experiments that require a septum magnet downstream of the target to bend scattered electrons to the minimum acceptance angle of the Hall A spectrometer arms. The magnet itself is not new and had been used during the running of PREX-1 at a nominal current of 377 A, which is well within the linear range of its operation. The septum field response is expected to be non-linear at high currents as magnetic saturation of the steel components in the magnet sets in. Since the CREX experiment runs at a beam energy of 2.2 GeV, to achieve the specified bend radius the septum magnet is required to provide a vertical dipole field that is more than double in magnitude that of PREX and where magnetic saturation in the return yoke and beam pipe shield is expected. The non-linear behaviour of the septum magnet was characterized to determine that the magnet meets the CREX field specifications. This makes it possible to run PREX-2 and CREX back-to-back without a configuration change. Further, the shield extension is shown to minimized the fringe field in the beam pipe to acceptable levels.

The field data were obtained from simulations of the septum field in which the non-linear PDE was solved by the Tosca FEA algorithm. This algorithm is based on a finite element formulation of the magnetic system that requires a description of the magnet geometry and definitions of the finite element mesh and the magnetic properties of the materials. The septum model data set was created using the Opera 3D modeller software package. A fine mesh was used inside of the magnet air gaps and iron components to provide a greater accuracy in the estimation of the geometry and enable a good field quality in these regions. Due to the symmetries of the magnet, the finite element mesh was minimized to one quarter of the model which reduces the solution computation time. The septum field was simulated at 15 current density settings which cover the range of the magnet's operation. The model data set and Tosca FEA simulations are stored in a simulation database that are accessed through the Opera 3D post-processor software package.

The field response in the magnet gap was examined at a number of positions spanning the beam envelope acceptance region through the septum. At each position, an aggregate data set was compiled of 15 (I_i, B_{yi}) data pairs. Saturation of the field at high current is measured by the field deviation from the least-squares regression line of data in the linear region ($I \leq 500$ A) of the response curve. The Tosca simulations indicate that a third coil at each pole of the septum is necessary to achieve the field magnification required for CREX within the operational range of the magnet. Further, the rate of field saturation in the magnet gap is position dependent, this is evident from both the simulations and the empirical data, and is generally faster outward from the centre.

The septum field integral specified for CREX, that achieves a forward scattering angle of 3°, is 1.21 Tm. This requires a high coil current that is outside the range of operational experience. In order to confirm the current setting for CREX, the response curve of the central field integral was simulated by Tosca. With the post-processor software, the total field integral is evaluated from z=-100 cm to z=100 cm on the centre line of the magnet gap at every current density setting that was simulated, producing an aggregate data set of 15 (I_i, $\int B_i dz|_0$) data pairs. The septum achieves a central field integral of 1.193 Tm at $J = -1300$ A/cm^2. This corresponds to $I = 936$ A in the 3-coil magnet configuration, which is within the magnet's operational current range. Some vertical dispersion to electron trajectories is caused by B_x, which is non-zero off the centre line and warrants a measurement of the horizontal field integral in addition to the vertical one. Because the beam envelope will span a total area cross-section of 22 cm x 20 cm as it is transported through the magnet gap, the change in the component field integrals were examined within this total acceptance region. The maximum variation of the vertical field integral from 1.193 Tm is $\Delta \int B_y dz =^{+0.060}_{-0.155}$ Tm in the region -14 cm$\leq \tilde{x}$ <-10 cm and $\pm$0.060 Tm in the region -10 cm$\leq \tilde{x} \leq$8.2 cm. The maximum variation of the horizontal field integral from 0 Tm is $\Delta \int B_x dz = \pm 0.198$ Tm in the region -14 cm$\leq \tilde{x}$ <-10 cm and $\pm$0.065 Tm in the region -10 cm$\leq \tilde{x} \leq$8.2 cm.

The iron shield inside the septum magnet was designed to reduce the stray field lines at the beam pipe in order to minimize vertical and horizontal deflections of the high energy beam that is transported straight through. Tosca simulations show substantial magnetic saturation of the shield at current settings above 500 A. The total field integral in the beam pipe varies $\pm$0.163 Tm at the CREX current, which is 3 times the linear prediction. A new shield was proposed with an extension at the upstream and downstream magnet edges to mitigate the effect of shield saturation at the beam pipe. Analysis of the stray field lines inside the extended shield shows a reduction of the maximum fringe field at the upstream and downstream magnet edges of approximately 96% and 86%, respectively. The total field integral in the beam pipe varies $\pm$0.0164 Tm at the CREX current inside the extended shield. This is comparable to the maximum field integral inside the original shield at the PREX-2 current setting, which was acceptable for the PREX-1 experiment.

In order to meet the CREX specifications, the septum magnet will need to be configured with 3 coils at each pole. At current settings above 500 A the septum field response is non-linear due to magnetic saturation in the return yoke. Although some field saturation is evident at the CREX current setting, the septum magnet can reach the required dipole field integral within the acceptance zone of the beam envelope. The PREX-2 current setting is well within the linear range of the magnet's operation. Tosca simulations show substantial magnetic saturation in the shield at current settings above 500 A. The extension of the shield at the upstream and downstream magnet edges provides significantly better shielding inside the beam pipe and should be sufficient to keep radiation in the Hall below acceptable levels. In conclusion, the same septum magnet can be used for PREX-2 and CREX and therefore it is feasible to run the experiments back-to-back without a configuration change.

References

[1] K. S. Kumar, "Electroweak probe of neutron skins of nuclei," *Annals of Physics*, vol. 412, p. 168012, 2020.

[2] C. J. Horowitz, S. J. Pollock, P. A. Souder, and R. Michaels, "Parity violating measurements of neutron densities," *Phys. Rev. C*, vol. 63, p. 025501, Jan. 2001.

[3] S. Ban, C. J. Horowitz, and R. Michaels, "Parity violating electron scattering measurements of neutron densities," *Journal of Physics G: Nuclear and Particle Physics*, vol. 39, p. 015104, Nov. 2011.

[4] C. J. Horowitz, K. S. Kumar, and R. Michaels, "Electroweak measurements of neutron densities in crex and prex at jlab, usa," *The European Physical Journal A*, vol. 50, p. 48, Feb. 2014.

[5] S. Abrahamyan *et al.*, "Measurement of the neutron radius of ^{208}Pb through parity violation in electron scattering," *Phys. Rev. Lett.*, vol. 108, p. 112502, Mar. 2012.

[6] M. Aghasyan *et al.*, "Prex-ii: Precision parity-violating measurement of the neutron skin of lead." Proposal to Jefferson Lab PAC 38, unpublished, hallaweb.jlab.org/parity/prex, 2011.

[7] K. Allada *et al.*, "Crex: Parity-violating measurement of the weak charge distribution of ^{48}Ca to 0.02 fm accuracy." Proposal to Jefferson Lab PAC 40, unpublished, hallaweb.jlab.org/parity/prex, 2013.

[8] J. Rosenzweig, *Fundamentals of Beam Physics*. Oxford: Oxford University Press, 2003.

[9] H. Wiedemann, *Particle Accelerator Physics*. Graduate Texts in Physics, Cham: Springer Open, 4th ed., 2015.

[10] J. J. Livingood, *The Optics of Dipole Magnets*. Academic Press, 1969.

[11] C. T. Services, *Opera-3d Reference Manual Version 15R3*. Vector Fields Software, Oxford, England, 2012.

[12] J. Simkin and C. Trowbridge, "Three-dimensional nonlinear electromagnetic field computations using scalar potentials," *IEE proceedings. Part B, Electric power applications*, vol. 127, no. 6, pp. 368–, 1980.

[13] J. N. Reddy, *An Introduction to the Finite Element Method*. McGraw-Hill Education, 1984.

[14] P. Bevington and D. Robinson, *Data Reduction and Error Analysis for the Physical Sciences*. McGraw-Hill Education, 2003.